# LOCAL AND GLOBAL DEFORMATION FROM SYNCROTRON IMAGING OF CLOSED CELL FOAMS IN COMPRESSION

NICHOLAS BRANDON PHELPS

BACHELOR OF SCIENCE

Oklahoma State University

Stillwater, Oklahoma

May, 2005

Submitted to the Oklahoma State University
Graduate Office in partial Completion of
the degree of Master of Science
May, 2008

LOCAL AND GLOBAL DEFORMATION FROM
SYNCROTRON IMAGING OF CLOSED
CELL FOAMS IN COMPRESSION

Thesis Approved:

Jay C. Hanan
Thesis Advisor

Hongbing Lu

James E. Smay

A. Gordon Emslie
Dean of the Graduate College

1 Introduction ..... 1
1.1 Objectives ..... 1
1.2 The compressive properties of foams ..... 1
1.2.1 The linear elastic region ..... 3
1.2.2 The plateau region ..... 4
1.2.3 Densification of foams ..... 5
1.3 Applications of foams ..... 5
1.4 Processing foams ..... 6
1.4.1 Polymer Foam ..... 7
1.4.2 Metal Foams ..... 7
1.4.3 Bulk metallic glass foams ..... 9
2 Compression Testing ..... 14
2.1 Static Compression ..... 15
2.1.1 Static Compression testing of the PMI foam with the Diffraction–Tomography Materials Tester ..... 17
2.1.2 Static Compression of the BMG foam ..... 28
2.2 Dynamic compression of the BMG Foam ..... 29
3 Probing deformation with radiography and tomography ..... 32
3.1 Radiographic imaging ..... 32
3.1.1 Radiography of a specimen during compression ..... 34
3.1.2 Subtracting the background from radiographs ..... 35
3.1.3 Strain from real-time radiography ..... 38
3.2 Tomographic imaging ..... 41
3.2.1 Tomography of a specimen under stress ..... 42
3.2.2 Absorption vs. phase contrast ..... 43
3.2.3 Processing the tomographs for analysis ..... 46
3.2.4 Damage assessment ..... 55
3.2.5 Measuring two-dimensional strain ..... 57
3.3 Modeling and validation of stress predictions ..... 60
3.3.1 Analytical models ..... 61
3.3.2 Generalized Interpolation Material Point Method ..... 67
4 Conclusions ..... 71
5 Future Work ..... 72
References ..... 76

Figure 1: Optical image taken from the axial direction of a Bulk Metallic Glass foam.... 2
Figure 2: The typical stress-strain response for a elastic-plastic polymer (PMI) foam. .... 3
Figure 3: The images shown on the left are a surface rendered view of a Bulk Metallic Glass foam which illustrates the brittle behavior of cell walls. The tomograph of a polymer (PMI) foam is shown on the right and shows the local buckling of cell walls, which is typical nature for elastic-plastic foams. ..... 5
Figure 4: Optical image of the surface of the 86% porosity BMG foam [Luo 2007]..... 11
Figure 5: The Instron material tester compression setup with the extensometer attached directly to the compression platens. ..... 15
Figure 6: Stress strain plots from an MTS machine, Instron machine, and the diffraction load frame with radiographs and images. All samples were a 70% porosity PMI foam. ..... 16
Figure 7: Stress-strain graph of the PMI foam, zoomed in to calculated the experimental elastic modulus..... 17
Figure 8: The exploded view of the Diffraction-Tomography Materials Tester. ..... 19
Figure 9: Load frame mounted over the translation stage at ID-2-BM ..... 21
Figure 10: Schematic of the load frame arrangement and the X-ray imaging camera .... 22
Figure 11: Control and Data Acquisition Software Interface ..... 22
Figure 12: The hardware setup used to control and acquire data from the load frame. Components shown in the picture are: the load frame, SC-2345 (for signal conditioning and data acquisition), FW-7344 (controls the motor driver), Primatics (motor driver), laptop, and associated cables. Sufficient cabling is needed to reach from the frame to the controllers in the hutch without interference. ..... 24
Figure 13: User interface for controlling the load frame motor..... 26
Figure 14: Data acquisition user interface. ..... 26
Figure 15: Tomography load control user interface. ..... 27
Figure 16: SHPB experimental setup. [Luo 2007]..... 30
Figure 17: Images taken during the dynamic testing of the 83% porosity BMG foam from the unconfined test. ..... 31
Figure 18: The stress-strain curves from the dynamic testing of the bulk metallic glass foam. One sample was not confined while the other was with a copper tube. ..... 31
Figure 19: Basic X-ray imaging setup used at the Advanced Photon Source at Argonne National Lab..... 33
Figure 20: The monochromator setup used at the Advanced Photon Source Beamline 2-BM. ..... 34
Figure 21: Image of the background, produced from the monochromator without a sample in the path of the X-ray beam. Thousands of photons are available even in the dark regions of the image. ..... 35
Figure 22: Radiograph of the polymer foam with the background from the monochromator in the image, the raw signal. ..... 36
Figure 23: The resulting image after subtracting the background. ..... 37
Figure 24: Edge detector setup using NI Vision Assitant 7.1..... 39

Figure 25: Measuring strain from radiographs with NI Vision. ..... 40
Figure 26: Experimental setup at Advanced Photon Source. The monochromated beam is narrowed with the beam apertures then passed through the sample. A scintillator is used to transfer the X-rays to visible light, which is then focused onto the tomography CCD [Wang 2001]. ..... 42
Figure 27: Stress-strain graph of the PMI foam with the tomography data sets locations labeled by circles. ..... 43
Figure 28: Tomograph of the PMI foam with a zoomed in portion, which shows the edge enhancement due to phase contrast. ..... 45
Figure 29: A plot of the intensitys across the line shown on the zoomed in portion of Figure 28. ..... 45
Figure 30: The histogram from one of the polymer foam images before it was balanced. The gray scale color bar is shown at the bottom of the histogram. ..... 48
Figure 31: The balanced histogram of the polymer foam and the resulting image. 0 corresponds to 0 in the original image and 255 corresponds to 17. Phase contrast leads to streaking in the reconstruction. ..... 49
Figure 32: Before and after images of the BMG foam from balancing the histogram. ... 49
Figure 33: Fast Fourier Transform of the original image before the histogram was balanced. The zoomed in portion is outlined with the red box. ..... 50
Figure 34: Each set of images contain a filtered tomograph of the polymer foam (A), the corresponding filtered Fourier Transform (B), and a close-up view of a cell wall (C). ..... 52
Figure 35: Each set of images contain a filtered tomograph of the polymer foam (A), the corresponding filtered Fourier Transform (B), and a close-up view of a cell wall (C). ..... 53
Figure 36: Each set of images contain a filtered tomograph of the polymer foam (A), the corresponding filtered Fourier Transform (B), and a close-up view of a cell wall (C). ..... 54
Figure 37: Local brittle failures in the bulk metallic glass foam shown via a 3-dimensionally rendered image from a tomograph. ..... 56
Figure 38: Local plastic failures in the polymer foam. ..... 56
Figure 39: Radiographs at 0 and 10% strain of the polymer foam, showing the difficulty in measuring strain in two dimensions without a clear landmark to follow. .. 57
Figure 40: Tomographs at 0 and 10% strain of the polymer foam. A cell is marked with the red arrow to demonstrate the effectiveness of measuring strains in 2-dimensions with tomographs. ..... 58
Figure 41: The deformation plane from the bulk metallic glass specimen. ..... 59
Figure 42: Close-ups of radiographs from the polymer foam. These images demonstrate the difficulty in determining 2-dimensional strains with radiographs. ..... 60
Figure 43: Elastic modulus versus time from the nanoindentation of a thick cell wall on the polymer foam. The inset illustrates nanoindentation being performed on a cell wall of the polymer foam, which has an average cell size of 0.3 mm. [Daphalapurkar, 2007] ..... 62
Figure 44: Geometry of the tetrakaidecahedral cell. ..... 63
Figure 45: General stress-strain curve of the polymer foam with the predicted elastic modulus ($E^*_{pred}$) and the one determined experimentally ($E^*_{exp}$) ..... 65

Figure 46: GIMP stress-strain curve of the bulk metallic glass foam. ..... 68
Figure 47: Experimental stress-strain curve of BMG foam with 17% relative density... 69
Figure 48: GIMP stress-strain curve for the polymer foam. ..... 70
Figure 49. Example of a Ni metal lattice produced by robocasting. The plate can be formed in simple or complex shapes with negligible effect on the processing cost (for the same volume). Thus, plate armor for extremities would also be achievable with this fabrication method. For this proposal similar structures will be designed with commercial BMG alloys or equivalent..... 72

# 1 Introduction

Since the early days of the blacksmith, metals have been modified by alloying in effort to improve material properties to fit specific needs. For instance, steels have been alloyed with varied amounts of chromium, manganese, and silicon improving the corrosion resistance, strength, and oxidation, respectively [ASM[1] 1990]. The alloying of steels has manipulated the yield strengths from 200 to 1500 MPa and the fracture strengths from 500 to 2000 MPa [Gibson and Ashby 1997 pg.76-77]. Adjusting the amounts of each alloying element is responsible for these wide ranges, but there are properties that these changes cannot significantly affect. For example the Young's Modulus for steel alloys only ranges from 190 to 210 GPa, but by foaming a steel alloy the modulus could potentially be reduced to 10 GPa. Thus, foaming materials greatly affects material properties.

Foams are cellular structures that can be made from a wide variety of materials. Current processing methods, to make foams, randomly place cells throughout the sample making a complex microstructure. These remarkable microstructures provide their foamed samples with the mechanics needed for excellent energy absorption by increasing toughness and decreasing the Young's modulus. The toughness is the amount of energy that a sample can absorb before failure and the Young's modulus is the slope of the

elastic portion of the curve [Callister 2000]. These properties of foams are at their best under compression.

## 1.1 Objectives

- Aid in the production of amorphous metal foams using powder metallurgy methods.
- Characterize BMG foam mechanical properties for the purpose of understanding their deformation and possible optimization of mechanical performance.
- Improve analysis methods, particularly those based on synchrotron imaging, in order to produce and test mechanical simulations of foam deformation.

## 1.2 The compressive properties of foams

The compression testing of foams is performed similar to that of solid specimens. The American Society for Testing and Materials (ASTM) has a standard for compressing rigid cellular plastics, which has some differences from the standard for compressing solid samples [ASTM E 9, ASTM D 1621]. Some specific differences include, the standard for cellular materials does not list tolerances for the parallelism of the compression platens or sample and the surface finish of the sample is also not specified. Such requirements are unnecessary or impossible with foam specimens.

Despite the similarities, between solid and foamed specimens in testing, there are major differences between the stress-strain curves. The buckling of a solid cylindrical sample is not considered a factor until the length to diameter ratio exceeds 3 [ASTM E 9]; for

foamed samples, the ideal length to diameter ratio is ≤ 1 [ASTM D 1621]. At the ideal length to diameter ratio for solid and foamed samples, buckling of the sample globally is not a consideration, but at the ideal length to diameter ratio, foamed samples often exhibit buckling locally in the sample.

The processing methods of most foams give each sample a unique and random microstructure (Figure 1). Similar to grain structures in solids, the microstructure varies between foam samples. The global properties of foams are consistent between samples when a large enough region is used, which has been shown in computational simulations [Ma 2006].

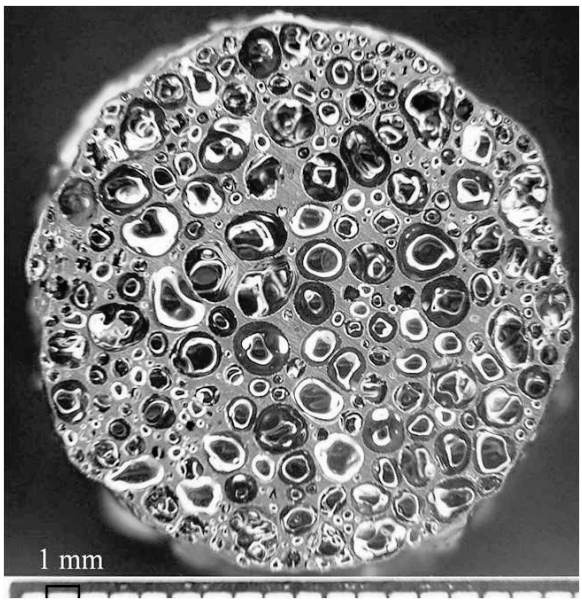


**Figure 1: Optical image taken from the axial direction of a Bulk Metallic Glass foam.**

The compressive stress-strain curves of cellular materials, like solid samples, have a linear elastic region but they also exhibit a plateau region and upon high strain levels the cellular samples densify. These unique characteristics in their compressive loading

curves lend to the utilization of foams in energy absorbing circumstances. Figure 2 is the stress-strain curve of a polymer foam sample under compression [Daphalapurkar *et al.* 2007].

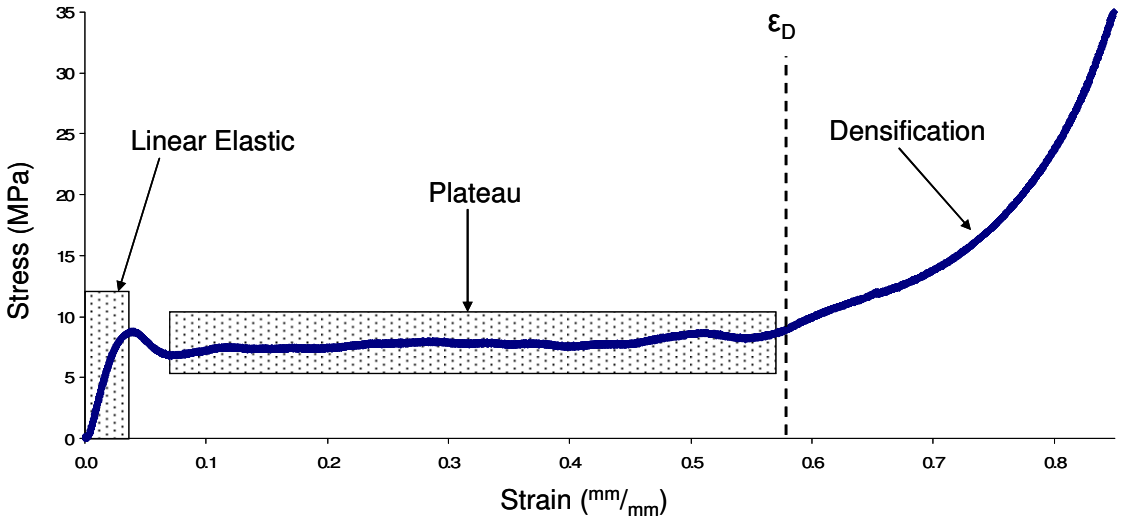


**Figure 2: The typical stress-strain response for a elastic-plastic polymer (PMI) foam.**

### 1.2.1 The linear elastic region

The Young's Modulus associated with foamed materials is linear like that of solid materials, but they do not have the same modulus as their parent material. Due to the complex structures of foams it is not reasonable to calculate the exact area of the specimen in order to obtain its Young's Modulus (such an attempt would also require very short samples to avoid buckling); therefore, the modulus and applied stress are calculated by the outside diameter of the sample. The difference in the moduli between the foam and its parent material is intuitively obvious. Consider a cellular sample and a solid sample, both made of the same material. If both samples have the same outside

dimensions then the cellular sample will have a higher compliance than the solid sample during the elastic portion. Differences in the stress-strain curve arise since the cellular sample has less material due to its empty cells. The elastic region of cellular materials is dominated by elastic bending of cell walls and faces.

### 1.2.2 The plateau region

The plateau region of cellular stress-strain curves varies in height (stress) and total length (strain) based on the material, the type of cells (such as open or closed), and the relative porosity. The mechanisms which cause the plateau stress depend on the type of material. Elastomeric foams yield due to elastic buckling, elastic-plastic foams (as in Figure 2) yield from the formation of plastic zones at stress concentrations in the microstructure, and brittle foams yield due to the brittle crushing of their cells. Examples of brittle crushing and stress concentrations are shown in Figure 3.

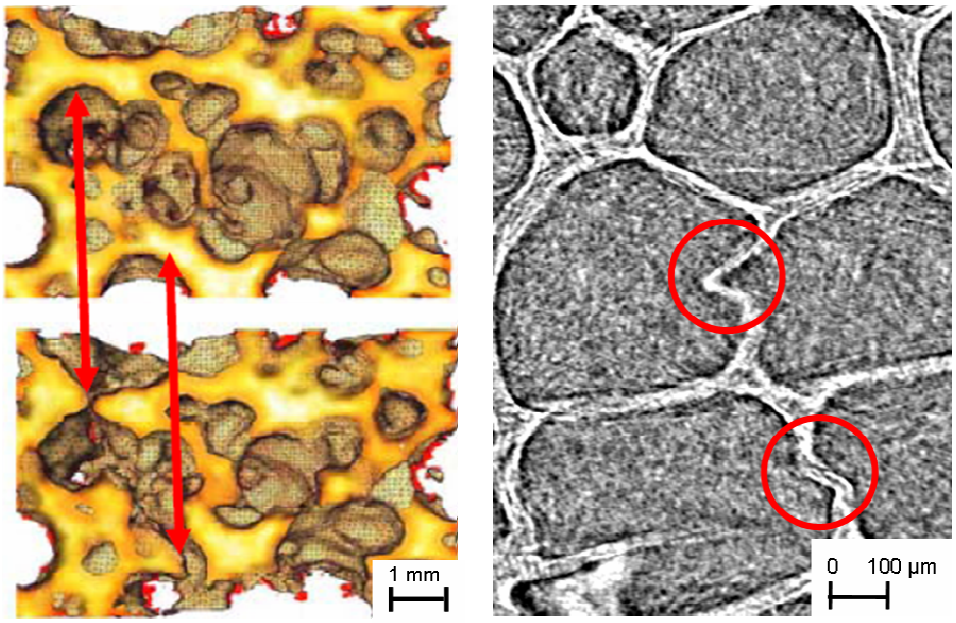


**Figure 3: The images shown on the left are a surface rendered view of a Bulk Metallic Glass foam which illustrates the brittle behavior of cell walls. The tomograph of a polymer (PMI) foam is shown on the right and shows the local buckling of cell walls, which is typical nature for elastic-plastic foams.**

### 1.2.3 Densification of foams

At some point, most foams will densify when compressed to strains beyond the plateau region. The resulting increase in stress is due to the collapse of cells and contact from the cell walls. Here the modulus approaches that of the solid. Exceptions to densification include the spalation of material commonly associated with compression of brittle foams. Confinement of the sample is important when considering densification and application of brittle foams.

## 1.3 Applications of foams

The process of foaming any material obviously reduces the density and, with the proper porosity and bulk material, the foam can be used as a thermal insulator, acoustic

insulator, packaging material, structural member or as an object that has high buoyancy properties [Gibson and Ashby 1997].

**Table 1: Applications of foams [Ashby 2000].**

| Application | Comment |
|---|---|
| Lightweight structures | Excellent stiffness-to-weight ratio when loaded in bending: attractive values of $E^{1/3}/\rho$ and $\sigma_y^{1/2}/\rho$ |
| Sandwich cores | Metal foams have low density with good shear and fracture strength |
| Strain isolation | Metal foams can take up strain mismatch by crushing at controlled pressure |
| Mechanical damping | The damping capacity of metal foams is larger than that of solid metals by up to a factor of 10 |
| Vibration control | Foamed panels have higher natural flexural vibration frequencies than solid sheet of the same mass per unit area |
| Acoustic absorption | Reticulated metal foams have sound-absorbing capacity |
| Energy management: compact or light energy absorbers | Metal foams have excptional ability to absorb energy at almost constant pressure |
| Packaging with high-temperature capability | Ability to absorb impact at constant load, coupled with thermal stability above room temperature |
| Artificial wood (furniture, wall panels) | Metal foams have some wood-like characteristics: light, stiff, and ability to be joined with wood screws |
| Thermal management: heat exchangers/ refrigerators | Open-cell foams have large accesssible surface area and high cell-wall conduction giving exceptional heat transfer ability |
| Thermal management: flame arresters | High thermal conductivity of cell edges together with high surface area quenches combustion |
| Thermal management: heat shields | Metfoams are non-flammable; oxidation of cell faces of closed-cell aluminum foams appears to impart exceptional resistances to direct flame |
| Consumable cores for castings | Metfoams, injection-molded to complex shapes, are used as consumable cores for aluminum castings |
| Biocompatible inserts | The cellular texture of biocompatible metal foams such as titanium stimulate cell growth |
| Filters | Open-cell foams with controled pore size have potential for high-temperature gas and fluid filtration |
| Electrical screening | Good electrical conduction, mechanical strength and low density make metfoams attractive for screening |
| Electrodes, and catalyst carriers | High surface/volume ratio allows compact electrodes with high reaction surface area |
| Buoyancy | Low density and good corrosion resistance suggests possible floatation applications |

## 1.4 Processing foams

Determining the optimum processing is dependent on the application, the type of material, and the desired microstructure of the material. Nature produces foams and cellular structures through many routes. Due to their low melting temperatures, moderate

reactivity, and compatibility with blowing agents; polymer foams have been successfully commercialized. The Styrofoam cup is ubiquitous and immediately recognized across modern cultures. Foam processing is so inexpensive that issues of recycling, land-fill use, and environmental contamination are common.

### 1.4.1 Polymer Foam

The polymer foam tested here is called Rohacell. "ROHACELL® is a polymethacrylimide- (PMI-) hard foam, that is used as a core material for sandwich constructions. It shows outstanding mechanical and thermal properties. "In comparison to all other foams it offers the best ratio of weight and mechanical properties as well as highest heat resistance." [Hauck 2007] The PMI foam is processed by a process called thermoplastic expansion, where a blowing agent is mixed into the molten polymer and then expanded under elevated temperatures [Ashby 2000].

### 1.4.2 Metal Foams

Metal foams are less common. Several companies such as: Cymat, Duocel, and Aporas, produce foams commercially, but costs prohibit many applications outside the laboratory [Ashby 2000]. For metal foams Ashby defines four broad processing classes (Met. Foams):

1. Formed from the vapor phase.
2. Electrodeposited from an aqueous solution.
3. Liquid-state processing.
4. Created in the solid state.

Nine Processes For Metal Foaming [Ashby 2000]

1. Bubbling gas through molten Al-SiC or Al-$Al_2O_3$ alloys.*
2. By stirring a foaming agent (typically $TiH_2$) into a molten alloy (typically an aluminum alloy) and controlling the pressure while cooling.*
3. Consolidation of a metal powder (aluminum alloys are the most common) with a particulate foaming agent ($TiH_2$) followed by heating into the mushy state when the foaming agent releases hydrogen, expanding the material.*
4. Manufacture of a ceramic mold from a wax or polymer foam precursor followed by burning-out of the precursor and pressure infiltration with a molten metal or metal powder slurry which is then sintered.*
5. Vapor phase deposition or electrodeposition of metal onto a polymer foam precursor which is subsequently burned out, leaving cell edges with hollow cores.
6. The trapping of high-pressure inert gas in pores by powder hot isostatic pressing (HIPing), followed by the expansion of the gas at elevated temperature.*
7. Sintering of hollow sphere, made by a modified atomization process, or from metal-oxide or hydride spheres followed by reduction or dehydridation, or by vapor-deposition of metal onto polymer spheres.
8. Co-pressing of a metal power with a leachable powder, or pressure-infiltration of a bed of leachable particles by a liquid metal, followed by leaching to leave a metal-foam skeleton.
9. Dissolution of gas (typical, hydrogen) in a liquid metal under pressure, allowing it to be released in a controlled way during subsequent solidification.*

Thermo-plastic expansion (as in 2, 3, 6, and 9 above) is based on a common method for expansion of polymer foams. Each process indicated by an "*" requires heating close to or above the melting point. For most metals, heating to the liquid state leads to low viscosity and a tendency for the porosity to become dominated by gravitational effects (floating bubbles) or escape altogether [Schroers *et al.* 2003]. Such difficulties have lead researchers to find alternatives as listed above.

Recently metals with the ability to maintain high viscosity for significant times near a glass transition temperature have been developed. These metals are called Bulk Metallic Glasses (BMG's) for their ability to be processed in sections as thick as 80 mm with cooling rates as slow as $1^{o}C/s$ [Liaw 2008]. These metals have been processed in similar ways to that of the polymer foams [http://www.liquidmetal.com/]. Thus, such alloys could solve the difficulty of processing metal foams using thermoplastic expansion.

### 1.4.3 Bulk metallic glass foams

Bulk metallic glasses (BMG) are amorphous metals with critical cooling rates low enough to allow formation of amorphous structure in thick layers, up to 12 millimeters [Peker and Johnson 1994]. In 2003, Schroers successfully foamed a BMG foam composed of $Pd_{43}Ni_{10}Cu_{27}P_{20}$ using hydrated $B_2O_3$ flux [Schroers *et al.* 2003]. In 2005, Brothers and Dunand developed the first BMG foam, which behaved plastically.

### 1.4.3.1 Single step thermo-plastic foaming

Some of the metal foams examined here used thermo plastic expansion. This can be done in one single step. A blowing agent is introduced as a powder while an ingot is softened so that the powder is mixed into the molten alloy. Once the mixture is underway the alloy is further heated so that the blowing agent is decomposed and the thermo-plastic expansion commences. Expansion must be complete and the foam quenched before crystallization occurs. Foams greater than 90% porosity have been made with this method in $Pd_{43}Ni_{10}Cu_{27}P_{20}$ BMG alloys. Blowing agents such as $B_2O_3$ [Demetriou *et al.* 2007] hydrate and $MgCO_3$ [Demetriou, *et al.* 2007] have been tested. This processing method was used to produce the 86% porosity foam used for dynamic compression discussed in Section 2.2.

This process expands the foam to conform to the shape of its container. In this case the container was a 19 mm diameter quartz tube. A precursor segment of equivalent mass is also presented alongside the foam in order to demonstrate the five-fold increase in volume produced by foaming. The foam naturally finishes with a closed wall about the sample as shown in Figure 4.

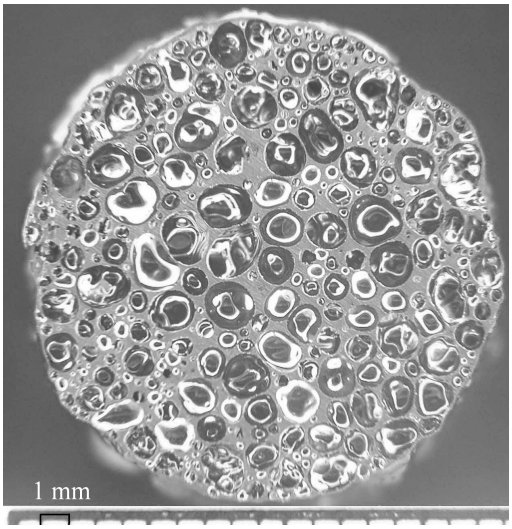


**Figure 4: Optical image of the surface of the 86% porosity BMG foam [Luo 2007].**

### 1.4.3.2 Two step thermo-plastic foaming

Similarly, a two step process can be used where a foam precursor is produced before thermoplastic expansion. The precursor is retained for later expansion at temperature. This method was used by Demetriou using a Pd, Ni, Cu based BMG alloy with a $B_2O_3$ hydrate powder precursor. The precursor was sealed in argon at 0.65 bar with the alloy in a quartz tube. The tube was then heated to 900℃ for 10 min. [Demetriou *et al.* 2006]. This is the process used for the BMG foams analyzed by tomography in the next chapters.

### 1.4.3.3 Powder HIPing and thermo-plastic foaming

Lastly, a method of two step thermo-plastic expansion foaming was explored where rather than softening the ingot for introduction of a blowing agent powder, the powders were mixed before consolidation using a Hot Isostatic Press (HIP). [Demetriou *et al.*

2007] So far, $Pd_{43}Ni_{10}Cu_{27}P_{20}$ BMG foams of 86% porosity have been produced using this route. Even lower densities are expected with further optimization of the process.

The method requires a careful mixture of BMG alloy powder with a blowing agent powder. Finer BMG alloys power should result in more even distribution of the cells, but contamination of the BMG alloy during processing is a concern so only limited crushing was attempted first. For this case, a uniform powder mixture with minimal segregation consisting of 95vol% $Pd_{43}Ni_{10}Cu_{27}P_{20}$ and 5vol% $MgCO_3$ was prepared. Hot Isostatic Pressing (HIP) was performed to consolidate the mixture (American Isostatic Presses, AIP6-30H). A stainless steel canister (19.05 mm in diameter and 65 mm in length) containing the powder mixture was first evacuated and then e-beam welded. A pressure of 207 MPa was first applied followed by a gradual temperature rise to 290±10 ºC—a temperature below the glass transition temperature. The mixture was held at the process temperature under the applied pressure for 2 hours. The canister was then cooled at pressure followed by release of pressure. The density of the consolidated precursor (measured by the Archimedes method) was the same as the monolithic solid to within measurement error (9.34±0.01 g/cc).

Expansion of the consolidated precursor into foam was performed by inductively heating the precursor to a temperature within the supercooled liquid region (below the crystallization temperature of 400$^{o}$C) under vacuum, holding for a period shorter than the time required for crystallization at that temperature, and subsequently quenching. Porosity was controlled by the temperature and duration of foaming. Various segments

of the precursor were expanded at temperatures ranging between 340 ºC and 370 ºC for durations ranging between 10 s and 100 s, accomplishing porosities that range between 4% and 86% (measured by the Archimedes method). A precursor segment of equivalent mass is also presented alongside the foam in order to demonstrate the five-fold increase in volume produced by foaming. [Demetriou *et al.* 2007]

This method shows further promise for application to higher strength alloys where an inert gas is used to introduce porosity. While a first attempt was unsuccessful, the alloy was evacuated when a purging vacuum was applied during HIP can preparation, a procedure has been established for testing this possibility. Similar to the above, a powder of BMG alloy is sealed in a stainless steel canister except in this case argon gas is pressurized in the can to 345 kPa (50 psi). Argon was used to avoid oxygen contamination of the alloy.

# 2 Compression Testing

Foams can have many purposes. A common mechanical application is energy absorbing in packaging or personnel protection. The energy absorbed by the sample is defined as the area enclosed by compressive stress-strain curve and the x-axis up to the strain limit of the test. Given an appropriately designed porosity, up to a limiting strain, the foam will never exhibit a stress greater than a safe value. Such energy absorption is equivalent to toughness measured in solids.

For energy absorption, foams are typically employed in a dynamic system. Therefore, an important test is to subject the sample to dynamic loads. However, it is not simple to determine the microstructural evolution during dynamic tests. Therefore, static tests were also run to help understand the microstructural aspects of the foam. The custom materials tester [Hanan *et al.* 2007] used for static testing was a recent development and results from this machine had not yet been compared with a machine calibrated according to ASTM specs. A materials tester with static compression capability[1] was used to compress a sample in effort to verify the static loading results from the custom diffraction/tomography materials tester.

[1] Instron 5800. 825 University Ave. Norwood, MA 02062. 800-473-7838

## 2.1 Static Compression

Compression tests were run on a traditional materials tester in order to verify the results from compression tests on the custom diffraction and tomography materials tester. The general setup is shown in Figure 5, where the extensometer is attached to the compression platens. The extensometer was attached directly to the compression platens to measure strain at the sample.

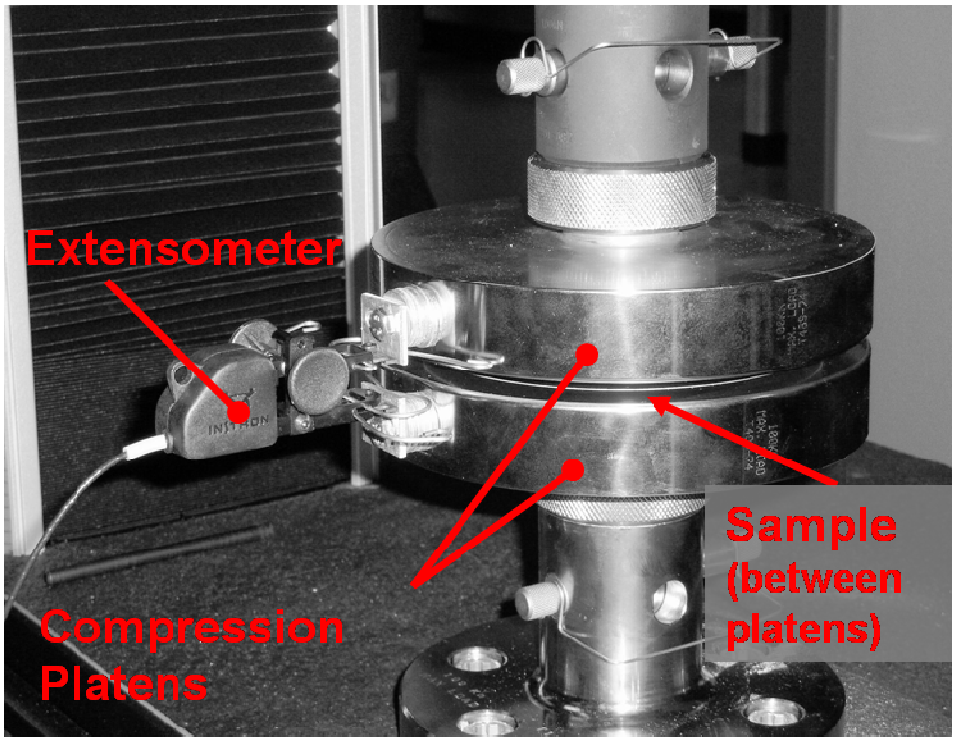


**Figure 5: The Instron material tester compression setup with the extensometer attached directly to the compression platens.**

The foam sample was compressed at a strain rate of 5% per minute and the data was compared to three other compression tests, two of which were done on the custom

diffraction/tomography materials tester (D/TMT) and the other on a MTS machine[2]. The comparison of the four stress strain curves is shown in Figure 6.

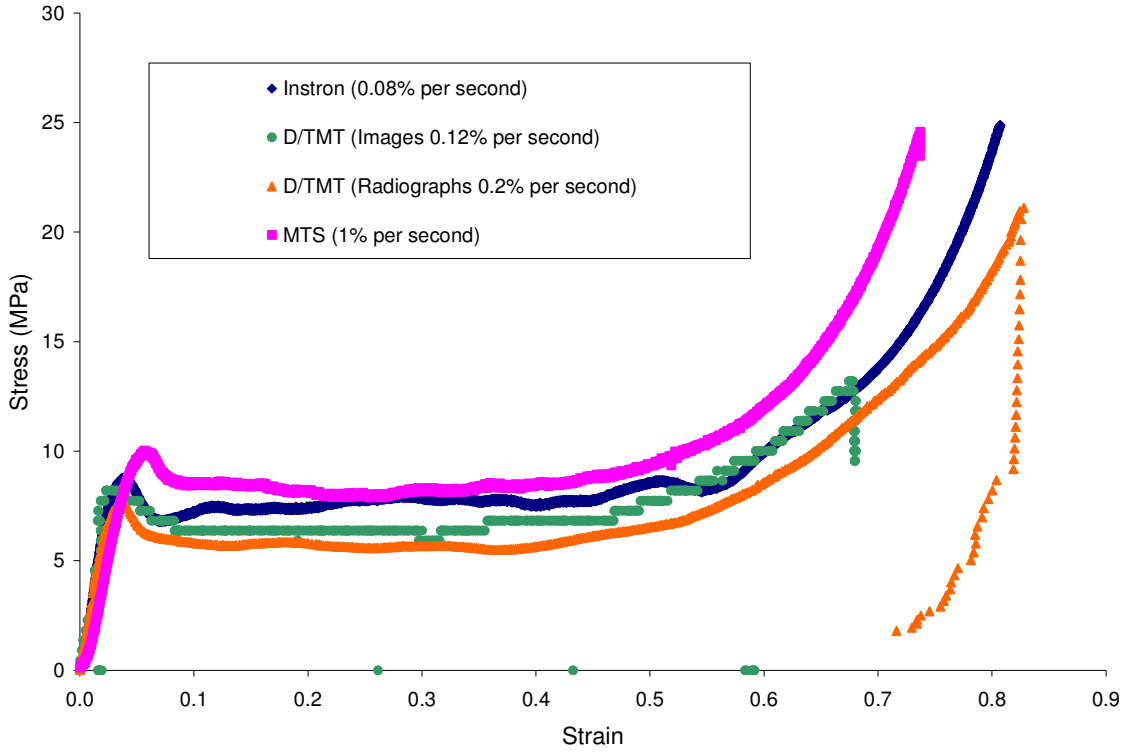


**Figure 6: Stress strain plots from an MTS machine, Instron machine, and the diffraction load frame with radiographs and images. All samples were a 70% porosity PMI foam.**

The data from the four curves are in agreement considering the PMI foam is made of a viscoelastic solid, which means the stress increases as a function of strain rate and depend on temperature. The modulus of elasticity was calculated from a linear set of points prior to yield as shown in Figure 7.

[2] MTS 14000 Technology Drive. Eden Prairie, MN 55344. 800-328-2255

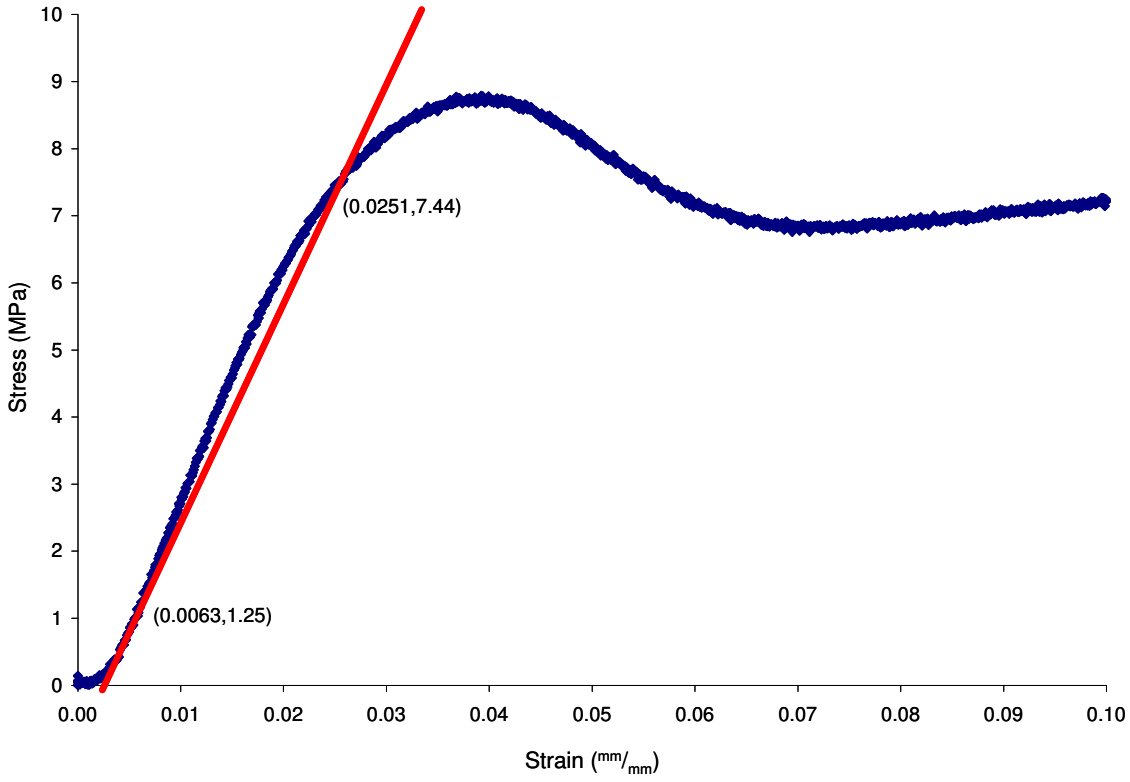


**Figure 7: Stress-strain graph of the PMI foam, zoomed in to calculated the experimental elastic modulus.**

### 2.1.1 Static Compression testing of the PMI foam with the Diffraction–Tomography Materials Tester

In order to apply controlled stress on the sample while monitoring the microstructure with X-ray radiography and tomography, a custom materials tester was built [Hanan, Bale, Phelps, "MATERIALS TESTER FOR IN-SITU DETERMINATION OF MECHANICAL and FATIGUE PROPERTIES USING X-RAY RADIATION" Patent Application, 2007]. Labeled the Diffraction/Tomography Materials Tester (D/TMT) the frame is also compatible with X-ray diffraction studies; however the diffraction capability was not used in the foam compression experiments.

**Highlights of the D/TMT** [Hanan Patent Application 2007]:

- The Basic purpose of the setup is to provide a capability of load application in a wide range of orientations i.e. tension, compression, bending, fatigue.
- Specialized for *in-situ* radiography/diffraction based imaging equipment which demands for a setup with no interruption of the incident X-ray beam while undergoing a 360º rotation about the sample axis. The unit is light weight, compact, and cost effective.
- The Materials Tester's supporting member is a transparent (low X-ray and visible light absorbing) polymer shell specially fabricated with considerations for diffracted portion of the beam.
- A specialized highly precise linear motor coupled with a high precision thread is the driving unit for load application. The motor is capable of short and long duration cycling without failure.
- The control system incorporated is a closed loop feed back type capable of controlling the load application based on a load feedback as well as a displacement feedback. The control system also has a remotely operable capability.

**Operation of the Materials Tester**

The invented device comprises of the top and bottom support plates and the transparent low absorption clear shell which form the basic load bearing structural unit when the experimental sample is being analyzed. The clear shell(3)forms a strong interference fit on the top plate(1) and bottom plate(2) and is also reinforced with a fastening collar. The top plate(1) bears the load application assembly consisting of the linear stepping

motor(5), the ultra fine threaded lead screw(8) and a support rod assembly(7) along with the brass anti-friction bearings(6). The free end of the lead screw(8) is coupled to an endplate which is also coupled to four support rods(7). This load application assembly is so designed that it can either apply a compressive or tensile load either in ramp mode or in cyclic mode.

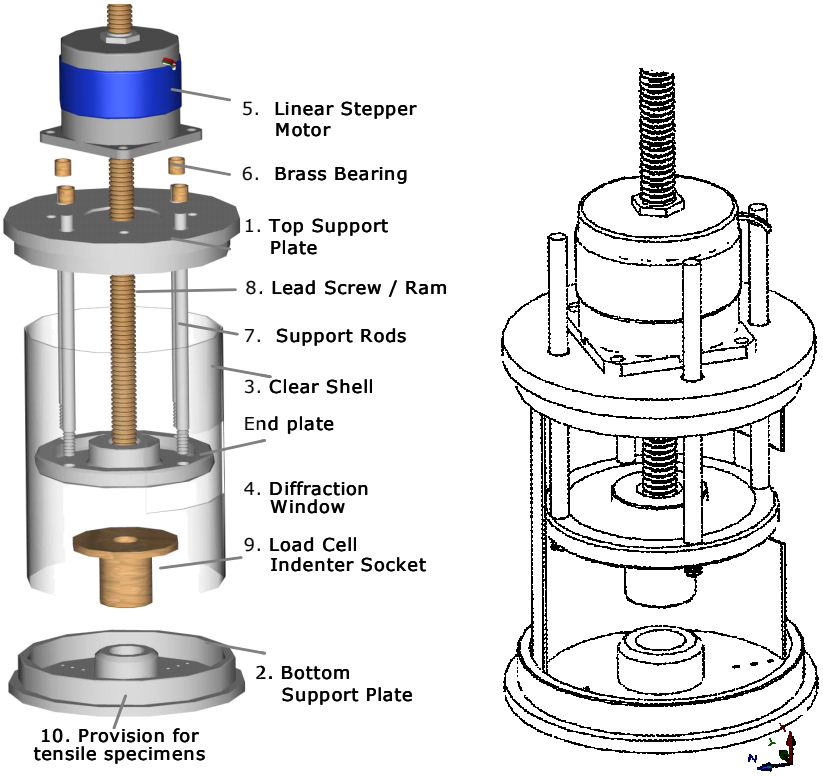


**Figure 8: The exploded view of the Diffraction-Tomography Materials Tester.**

The endplate plate has a provision for attaching a wide range of load applicators depending on the type of test being performed. The control software and motion control hardware transfer signal processed from the controller to the linear stepping motor which produces a linear motion of the applicator thus applying a load onto the sample. The support rods assist in bearing the transverse loads that tend to deflect the lead screw. The

linear movement of the lead screw is continuously tracked and fed back to the controller to control the motion when in displacement control mode. For a load controlled mode the operation relies on a load cell attached in series to the end plate. The fatigue cycling of the end applicator is software controlled and the motor is capable of small duty cycling with durations on the order of 5 cycles per second.

The lead screw design proves advantageous due to numerous reasons.

- The total stoke length of the end applicator can be the full length of the frame limited only by the length of the lead screw.
- The system is versatile for various sample sizes and a variety of tests.
- Better stability due to the assisting support rods.
- Possible torsional forces in the lead screws are eliminated due to the drive type being used.

The transparent polymer shell, which acts as a supporting frame, was chosen since it offers high transmission of the incoming as well as the transmitted X-ray beam. The absorption of the X-rays by the frame wall corresponds to approximately 10% of the total intensity. A diffraction window is provided on the frame for the diffracted beams to emerge out without any further interaction with the frame. The cross-head and grips are also designed with a provision for minimal shadowing of the diffracted radiation. Depending on target 2-θ and energy of the radiation this window may be repositioned.

The bottom plate(2) is fabricated with a tensile specimen mount which has a universal ball joint bearing provided for mounting tensile grips. The ball joint bearing minimizes bending loads. The bottom plate is also equipped with holes for mounting the device onto the translation stage of a standard Huber diffractometer. The mounted Materials Tester on a setup at ID-2-BM of the Advanced Photon Source is shown in Figure 3.

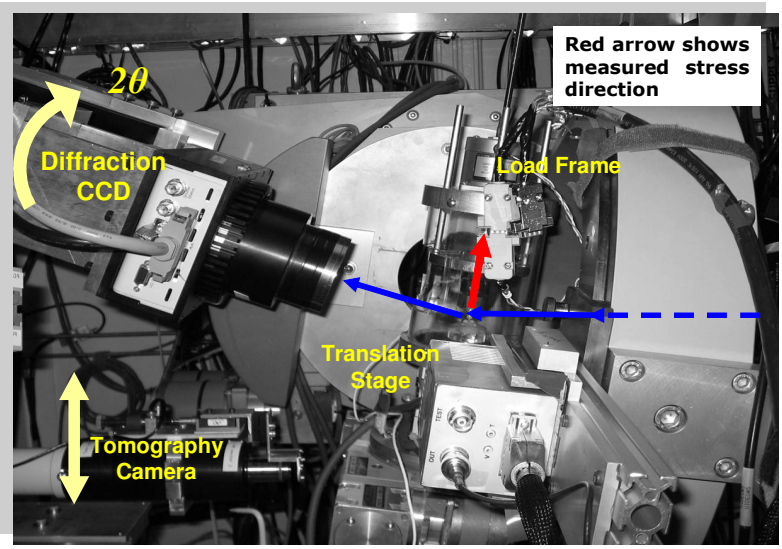


**Figure 9: Load frame mounted over the translation stage at ID-2-BM**

Samples mounting procedure: The test rig can accommodate various kinds of samples for tests in tension, compression, bending and fatigue cycling.

- Tensile specimens are gripped in specially fabricated grips. The sample is glued to the grips which have one threaded end and another with a shoulder. The threaded end is held by an adapter, which fits onto the load cell.

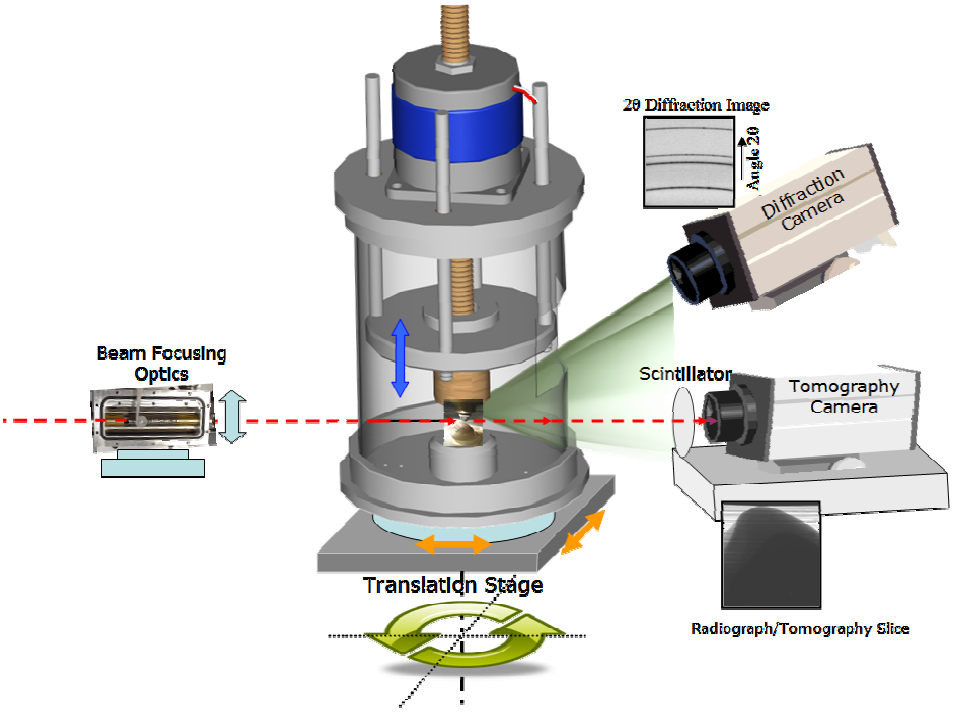


**Figure 10: Schematic of the load frame arrangement and the X-ray imaging camera**

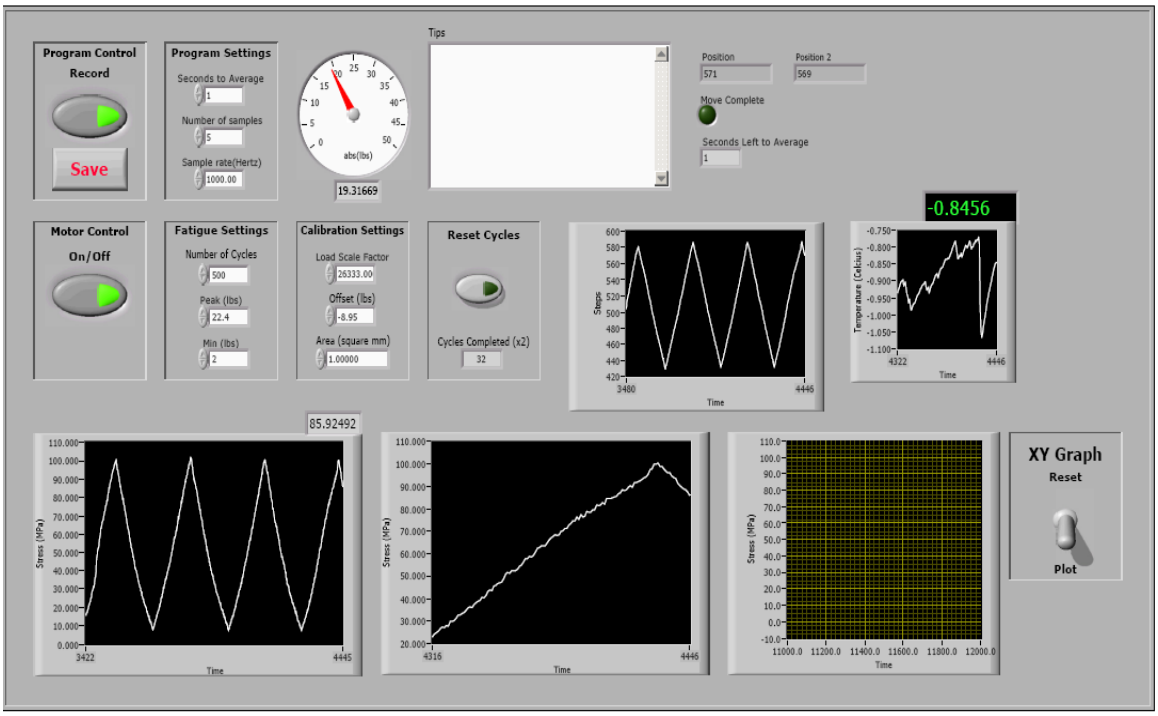


**Figure 11: Control and Data Acquisition Software Interface**

The control and sensing hardware interface for the custom materials tester consisted of two control boxes, a signal conditioning box, and a laptop. The motor movements were controlled by the two control boxes which consisted of a National Instrument, FW-7344 and a Primatics stepper motor driver. The Primatics motor driver was plugged into 120 VAC and directly into the FW-7344. The FW-7344 provides the communication link between the laptop and the motor driver. For signal conditioning, a National Instruments SC-2345 was used, readings included the raw voltage from the load cell (SCC-SG24) and thermocouple (SCC-TC01).

The displacement calculated from the stepper motor was run in a real-time open loop. More precise strains were calculated from radiographs. The software interaction with the hardware was done through LabVIEW. Custom programs were written to run the load frame. The general setup is shown in Figure 12.

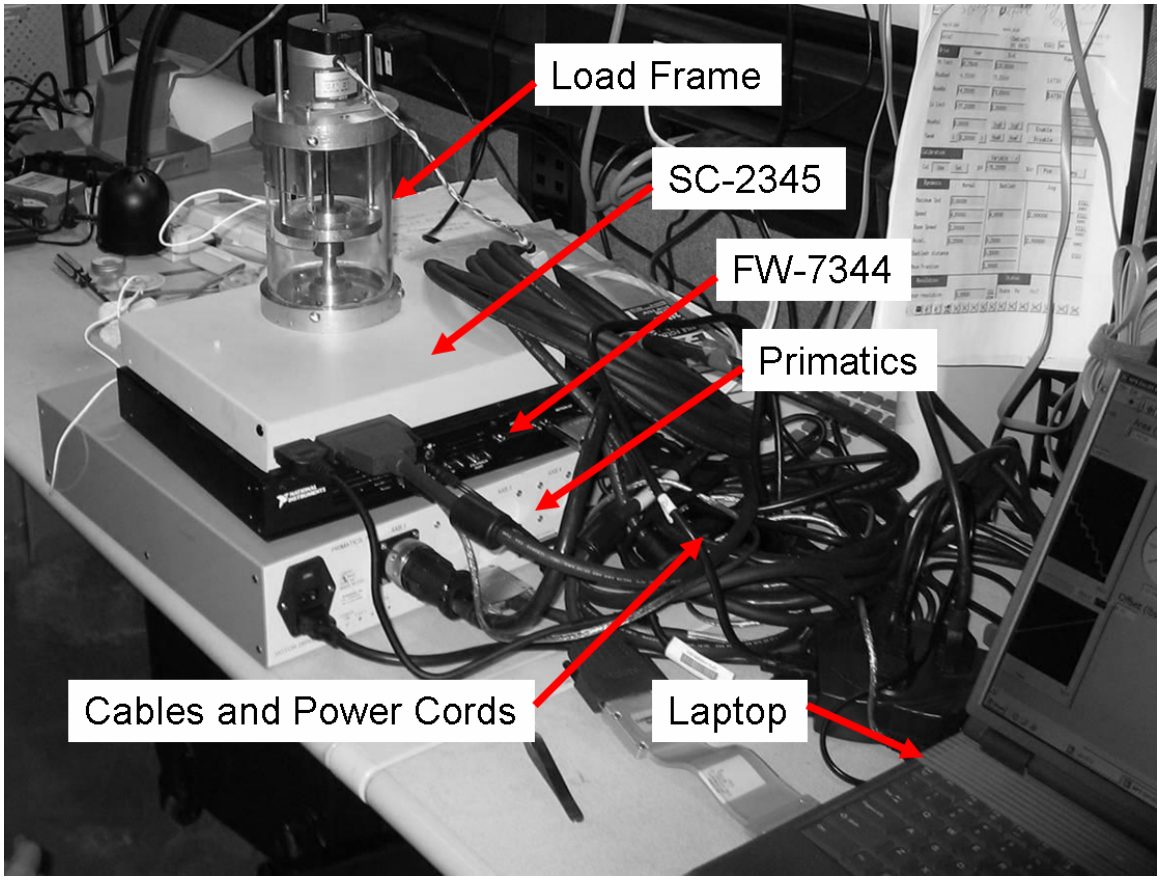


**Figure 12: The hardware setup used to control and acquire data from the load frame. Components shown in the picture are: the load frame, SC-2345 (for signal conditioning and data acquisition), FW-7344 (controls the motor driver), Primatics (motor driver), laptop, and associated cables. Sufficient cabling is needed to reach from the frame to the controllers in the hutch without interference.**

#### 2.1.1.1 Custom load control software

Determining the strain rate was decided by considering the target strain and the desired amount of time to run the test. Time to run the test depends on X-ray optical calculations such as exposure time per radiography. First the total desired strain was determined to be 70% based on densification of the foam and 60 minutes was decided for the total time to run the test with a 7 second exposure time per radiograph. The strain percentage was then multiplied by the gauge length of the sample then divided by the total time in order

to get the cross-head displacement per minute. Given the steps per revolution of the stepper motor and the threads per mm of the threaded shaft, the needed steps per minute was determined to be 6 steps per second as calculated in Equations 1- 3.

$$\left[\left(\frac{2000\ \text{steps}}{\text{revolution}}\right)\left(\frac{1\ \text{revolution}}{1\ \text{thread}}\right)\left(\frac{40\ \text{threads}}{25.4\ \text{mm}}\right)\right]^{-1} = \frac{0.318\ \mu\text{m}}{\text{step}} \tag{1}$$

For 70% strain on a sample with a 5mm gauge length:

$$0.7 * 5\ \text{mm} * \frac{\text{steps}}{0.318\ \mu\text{m}} = 11{,}024\ \text{steps} \tag{2}$$

$$\left(\frac{11{,}024\ \text{steps}}{60\ \text{min}}\right)\left(\frac{1\ \text{min}}{60\ \text{sec}}\right) = 3\ \text{steps}/\text{sec} \tag{3}$$

The speed setting along with the hardware configuration was done through the Measurement and Automation Explorer software (MAX) by National Instruments. MAX is a user interface to setup the control hardware for LabVIEW, which is the code that the control software was written in for the materials tester.

The software to control the materials tester during radiography and basic compression tests was split into two different programs in effort to simplify programming. One program was written to handle the motor control functions and the other was for data

acquisition. The user interface for the motor control program is shown in Figure 13 and the interface for the data acquisition is shown in Figure 14.

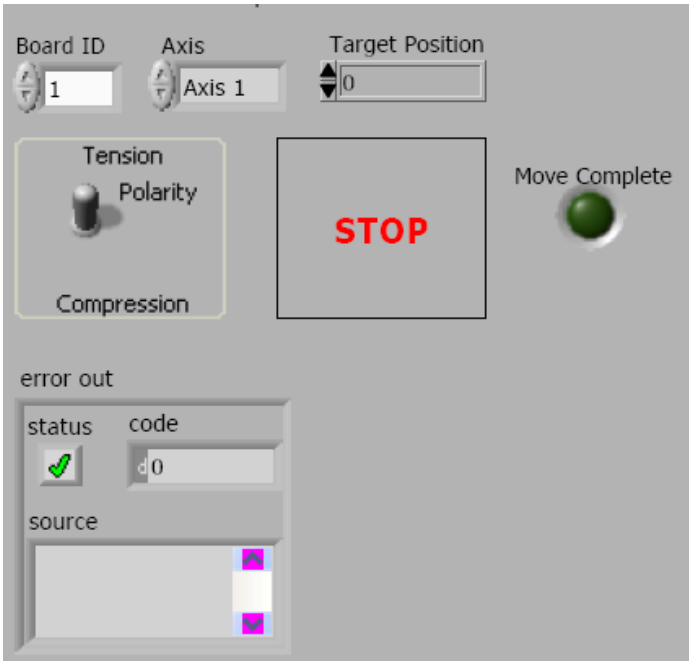


**Figure 13: User interface for controlling the load frame motor.**

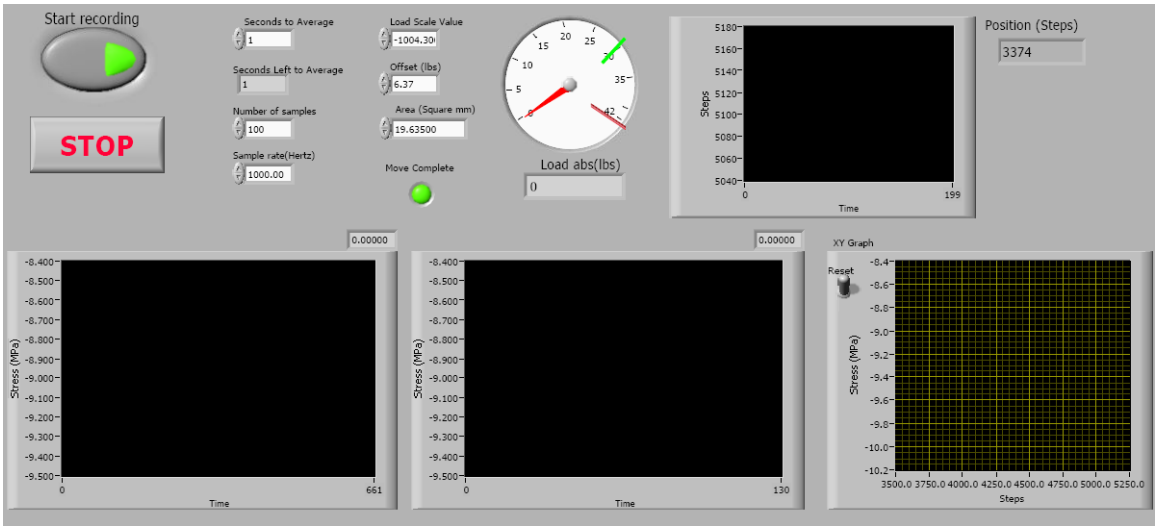


**Figure 14: Data acquisition user interface.**

The motor control program was designed with simplicity. The two most important features to the user in this program are the toggle for running tension or compression tests (motor direction) and a target position which is measured in steps.

The previously mentioned programs were also used for tomography; however, for tomography the load needs to remain constant during the scanning, which took about 3 hours per tomography scan. The motor control and data acquisition programs were used to control and monitor the load frame during compression between tomography scans. When the desired load was reached, both of those were terminated and the tomography load control program was initiated (Figure 15).

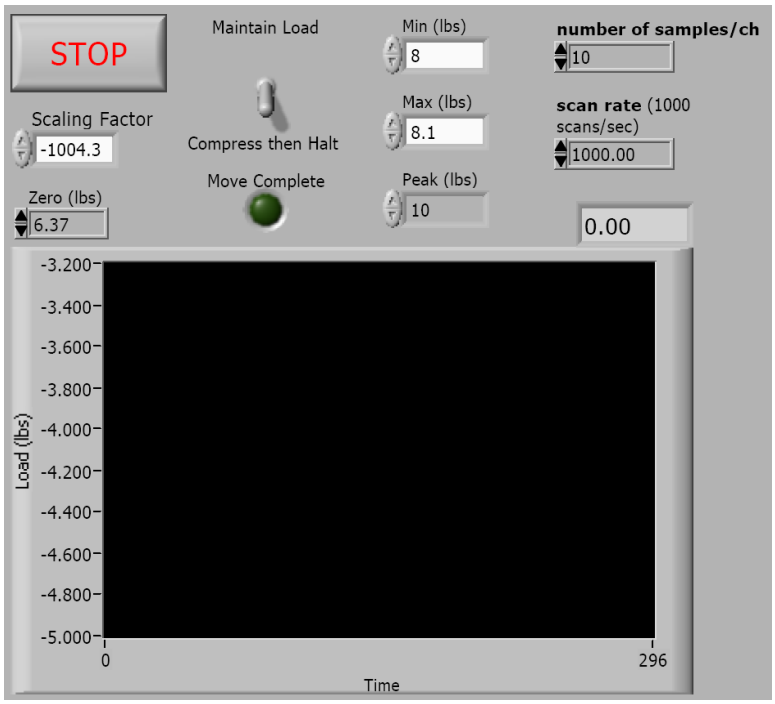


**Figure 15: Tomography load control user interface.**

The tomography load control program has several key features which should be noted. The "scaling factor" was determined during the calibration of the load cell and the value

was multiplied to the raw voltage from the load cell while "zero" was used to balance the load cell to a value of zero. The maximum and minimum values were used to create a window for the load which can easily be set to the users specified tolerances. Using a window for the desired load can prevent the motor from constantly running with a larger tolerance which keeps the motor cooler and extends the overall life of the motor.

As mentioned before (Figure 6), the strain curves given by this materials tester agree well with ASTM calibrated equipment.

### 2.1.2 Static Compression of the BMG foam

As with the polymer foam, static compression of BMG foam was conducted both in the beam and in a materials tester. Results of these compressive tests are shown here. While similar to the tests above on the PMI foam, including a tomographed sample at the same porosity, samples with multiple porosities were available for testing.

Compressive testing of [HIPed] foams with porosities of 4%, 40% and 86% was performed. Square specimens with polished and parallel loading surfaces having aspect ratios ranging between 1.0 and 1.5 were prepared. Strain rates of $1\times10^{-4}$ $s^{-1}$ were applied. Strains were measured using a linear variable displacement transducer. The 4% porosity foam is shown to yield at a relatively high stress (650 MPa), however is able to undergo only minimal plastic deformation before failing catastrophically by an incipient collapse event. The 40% porosity foam fails at a lower stress (225 MPa), however owing to the principal collapse being non-catastrophic, the foam is able to undergo considerable

plastic deformation at a plateau stress that is approximately 50% of the yield stress. It is interesting to note that the failure characteristics of the present 40% porosity foam are similar to the 40% porosity foam, which likewise fails by an incipient non-catastrophic collapse event characterized by a stress drop in excess of 30%. In contrast, the 86% porosity foam produced here yields at a considerably lower stress (25 MPa), however is capable of maintaining a plateau stress that is on average comparable to the failure stress. Consequently, as shown in Fig. 5, the 86% porosity foam is able to undergo plastic deformation to 80% strain approaching full densification (note that the densification strain for an 86% porosity foam can be estimated from established correlations to be ~80%). Due to a relatively high and, on average, constant plateau stress, the foam is able to absorb a considerable amount of mechanical energy prior to being fully densified. The specific energy absorbed by this foam can be estimated from the area under the stress-strain curve to be 31 $MJ/m^3$. [Demetriou *et al.* 2007]

Similarly, the 70% porosity BMG foam was processed by two-stage thermoplastic expansion [Demetriou (In Press)]. Its behavior is consistent with that observed by the other samples.

## 2.2 Dynamic compression of the BMG Foam

The first dynamic compression of bulk metallic glass foam was done using the Split Hopkinson Pressure Bar test (SHPB).[Luo, et al., Unpublished Results (2006)] A schematic for SHPB is shown in Figure 16.

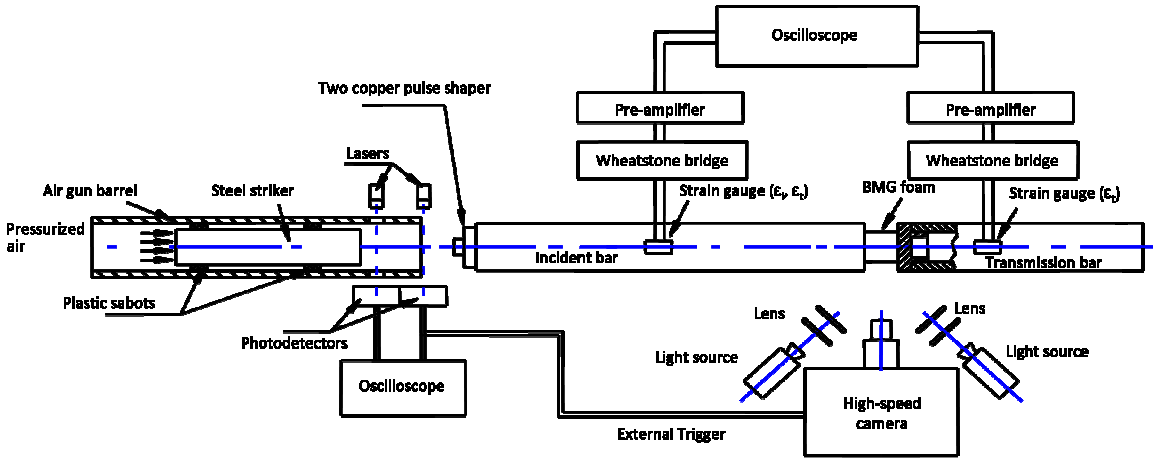


**Figure 16: SHPB experimental setup. [Luo 2007]**

The first sample tested dynamically was done without confinement. The sample was processed as a one-step thermoplastic expansion. It had a density of 86%. The sample was placed between the incident and transmission bars. Due to the brittle nature of the foamed sample, pieces broke off in every direction upon impact. The stress-strain curve for the unconfined tests is shown in Figure 18 along with the second confined test's stress-strain curve. For the confined impact test, the foamed sample was glued with an epoxy and alumina mixture inside a copper sleeve. The sleeve was added to confine the sample during impact. The thin (0.1") alumina epoxy layer was mixed at a ratio that approximated the modulus of the bulk metallic glass sample. Five frames from the unconfined dynamic testing of the 83% porosity BMG foam are shown in Figure 17.

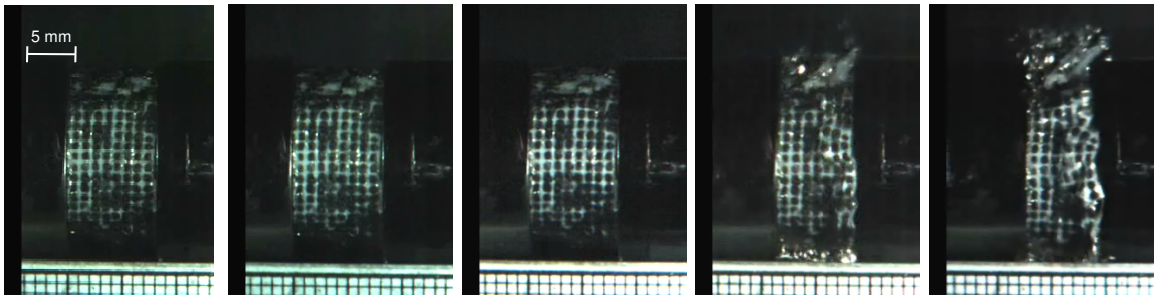


**Figure 17: Images taken during the dynamic testing of the 83% porosity BMG foam from the unconfined test.**

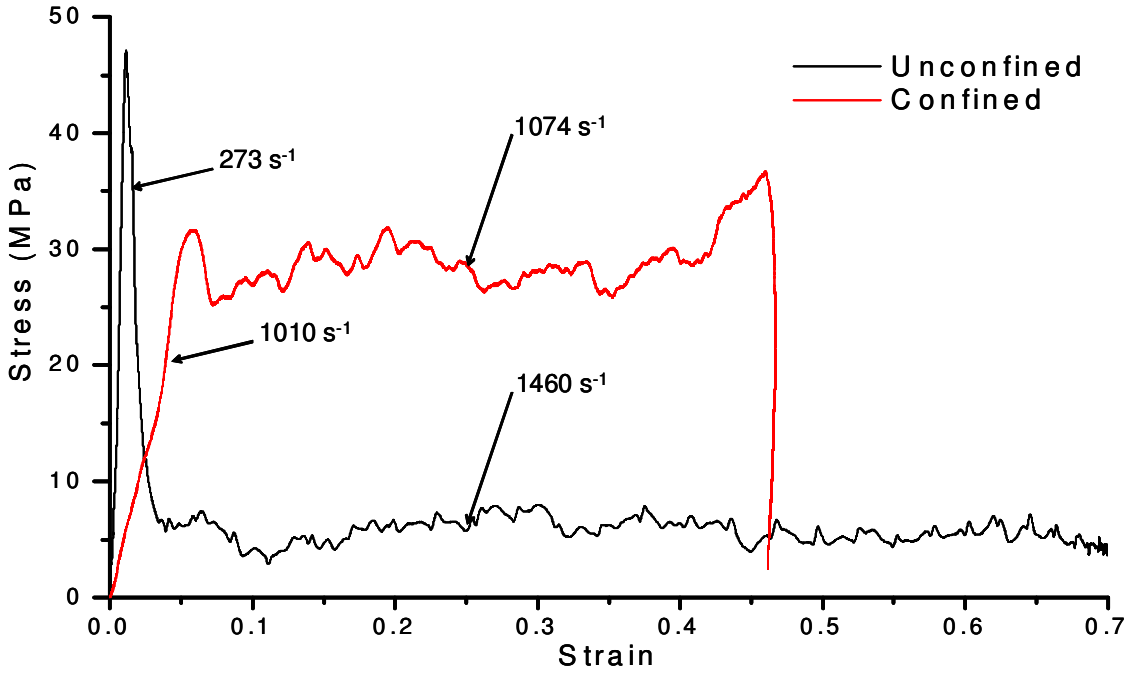


**Figure 18: The stress-strain curves from the dynamic testing of the bulk metallic glass foam. One sample was not confined while the other was with a copper tube.**

# 3 Probing deformation with radiography and tomography

In effort to better understand the failure mechanisms of foams, it is necessary to explore methods which enable visualization of the microstructure of the sample. Radiography and tomography enable visualization in two and three dimensions respectively. Both of these methods have benefits and disadvantages.

## 3.1 Radiographic imaging

Radiographic imaging is a relatively fast process when compared to tomography. Radiographic imaging is the process by where a picture is produced on a sensitive surface by a form or radiation other than visible light [Merriam 2007]. The setup used at APS is shown in Figure 19; where $I_o$ is the raw X-ray beam coming from the monochromator, $I$ is the X-ray beam carrying the information from the sample, and *Light* is the visible light, which comes from the single crystal phosphor.

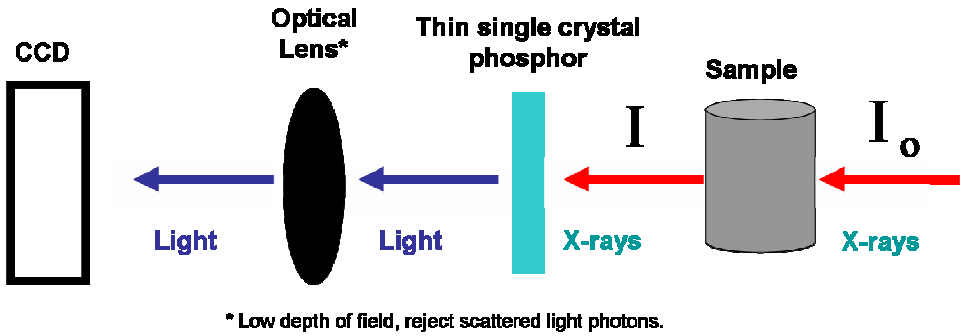


**Figure 19: Basic X-ray imaging setup used at the Advanced Photon Source at Argonne National Lab.**

The monochromator is used to extract a single wavelength from the incoming X-ray beam (as in Figure 20). Using a single wavelength enables the use of phase contrast and prevents beam hardening. As X-rays pass through materials, the higher energy X-rays are preferentially passed through the material while the lower energies are absorbed. This leads to apparent density reduction along the edges of thicker regions in homogenous samples. This error is called beam hardening, since the average value of the X-ray wavelengths is higher when passed through the sample [Bushberg 2002].

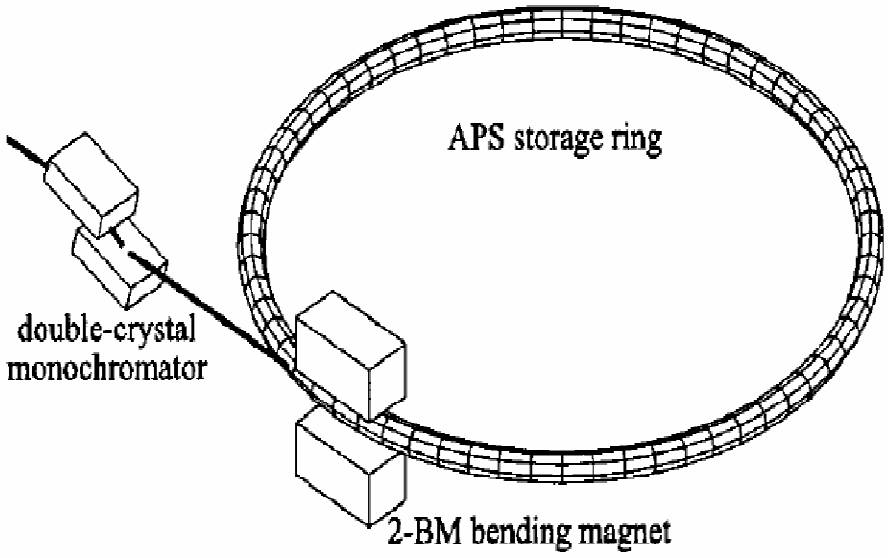


**Figure 20: The monochromator setup used at the Advanced Photon Source Beamline 2-BM.**

### 3.1.1 Radiography of a specimen during compression

Specimens can be radiographed during compression tests using a custom materials tester which allows X-rays to pass through the sample. The compression tests were done at a relatively slow strain rate ( 2.3%/min) which was discussed in section 2.1.1.1. A strain rate of this speed enabled the radiographs to be taken with little to no blurring from motion during exposure. The raw radiographs can be viewed immediately by converting the images to 8-bit, but the clarity of the images is greatly improved by subtracting the background.

### 3.1.2 Subtracting the background from radiographs

The background in the radiographs is due to the monochromator which was used to extract a single wavelength from the incoming X-ray beam as discussed in section 3.1. To get the clearest possible images from the radiographs the background image created by the monochromator should be subtracted. The image produced by the monochromator is shown in Figure 21. This image is referred to as the brightfield image and is the $I_o$ shown in Figure 19.

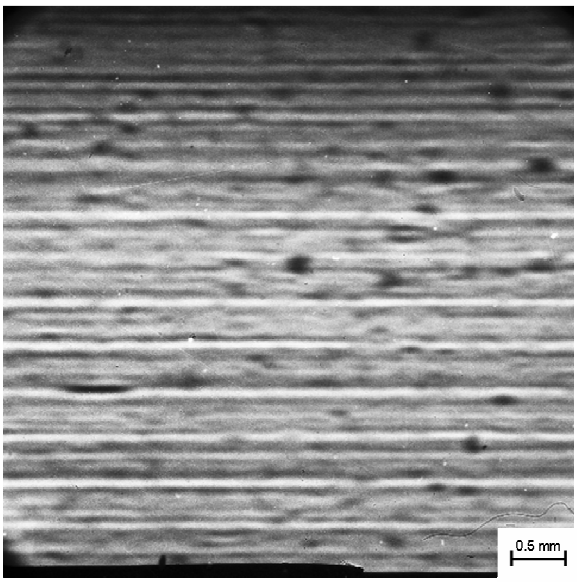


**Figure 21: Image of the background, produced from the monochromator without a sample in the path of the X-ray beam. Thousands of photons are available even in the dark regions of the image.**

Once the beam has passed through the sample it then carries the information of the sample along with the background, which corresponds to $I$ in Figure 19. Viewing the image with the background reduces apparent contrast. The raw radiograph of the polymer foam with the background is shown in Figure 22.

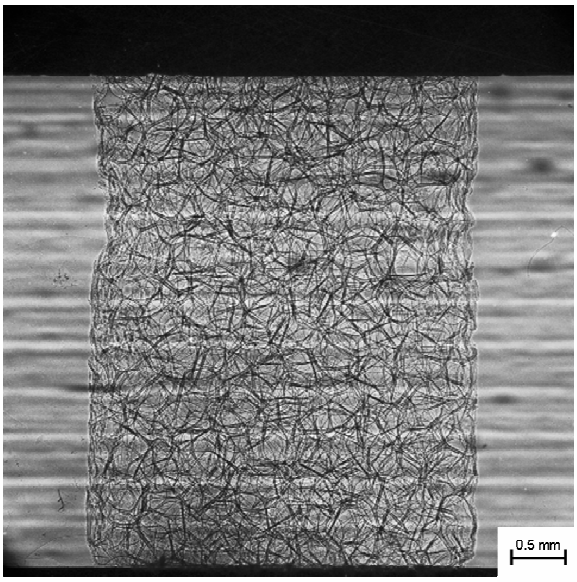


**Figure 22: Radiograph of the polymer foam with the background from the monochromator in the image, the raw signal.**

Removing the background created by the monochromator is known as subtracting the background. It is important to understand the relationship between the background, absorption of X-rays, and the resulting image to effectively remove the background. An approximation to the relationship between these is shown in equation 4; where $I$ is the resulting image, $I_o$ is the image of just the background, $\mu$ is the linear attenuation coefficient, and $t$ is the thickness of the material.

$$I = I_o e^{-\mu t} \tag{4}$$

This equation shows that the absorption of photons through a thickness of material has an exponential relationship with linear attenuation coefficient, and is used for pure absorption contrast. There is only purely absorption contrast when the foam is on the detector. As the distance between the foam and detector increases, there is an increasing

amount of phase contrast, which can appear as noise in radiographs and tomographs [De Carlo 2006]. The use of a monochromator was convenient since the linear attenuation coefficient is dependent on the incoming wavelength (λ). The foam's thickness can then be readily calculated by rearranging equation 4 to solve for *t* as shown.

$$t = -\frac{\ln\left(\frac{I}{I_o}\right)}{\mu} \tag{5}$$

With Figure 21 being the raw X-ray beam (*I*) and Figure 22 being the resulting X-ray beam ($I_o$) it is easy to subtract the background in the radiographs. The resulting image is a function of the material's thickness and is shown in Figure 23.

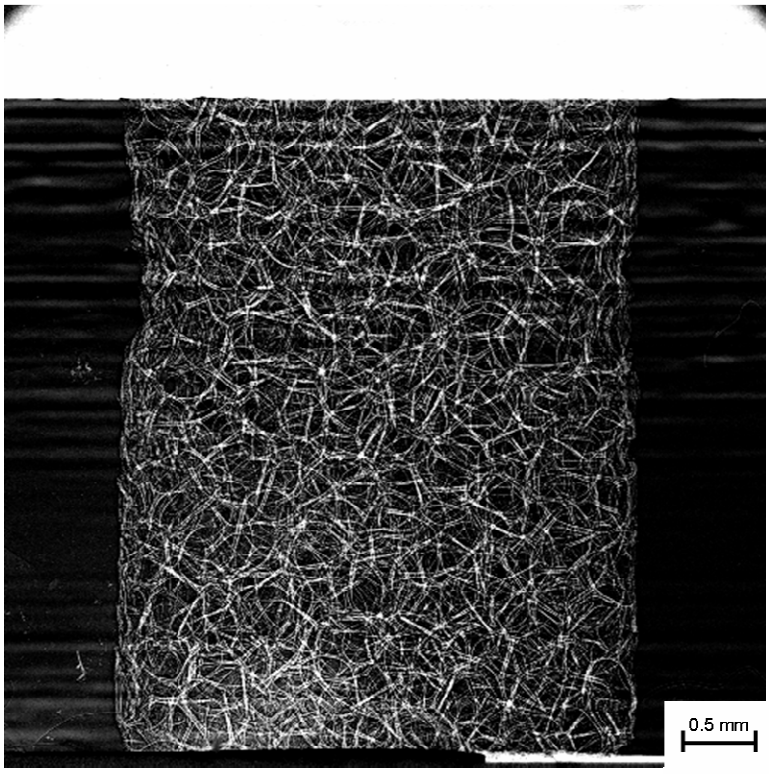


**Figure 23: The resulting image after subtracting the background.**

The foam shown in Figure 23 shows up as being white since the resulting radiograph is a function of thickness. This means that the thickest part of the foam is shown as a value of 255 and the air surrounding the foam is 0 (for an 8-bit image). The white band across the top of the image is from the crosshead of the load frame which made determining the global strains from the radiographs a simple procedure.

### 3.1.3 Strain from real-time radiography

The cross-head of the D-TMT can be seen accurately in the radiographs of the foam. This made the use of a standard machine vision edge detector an easy way to automate measurement of strain. Vision Assistant 7.1 from National Instruments was used to perform a batch process on the radiographs. The edge of the compression platen was detected using a line profile. The edge detection algorithm has five controls to refine the edge detection. During compression, the top compression platen was moving from the top of the screen downward while the bottom platen was fixed. The top platen was made of a solid piece of brass which showed up clearly in the radiographs. The vision software was set to find a horizontal line moving from top down. The gap specifies the number of pixels between search lines.

**Definitions for edge detection in Vision Assistant:**

- **Search Lines**
    - **Direction**—Direction in which you want the search lines to look for a straight edge within the region of interest.
    - **Gap**—Number of pixels between search lines in the region of interest.

- **Edge Strength**—Minimum difference in the intensity values between the edge and its surroundings.
- **Smoothing**—Number of pixels averaged to find the contrast at either side of the edge.
- **Steepness**—Maximum distance in which the edge strength must occur. Steepness characterizes the slope of the edge. Use a higher Steepness value to detect edges in images whose pixel intensities gradually transition from the background to the edge.

- **Edge Strength Profile**—Edge strength along the search line located in the middle of the region of interest.

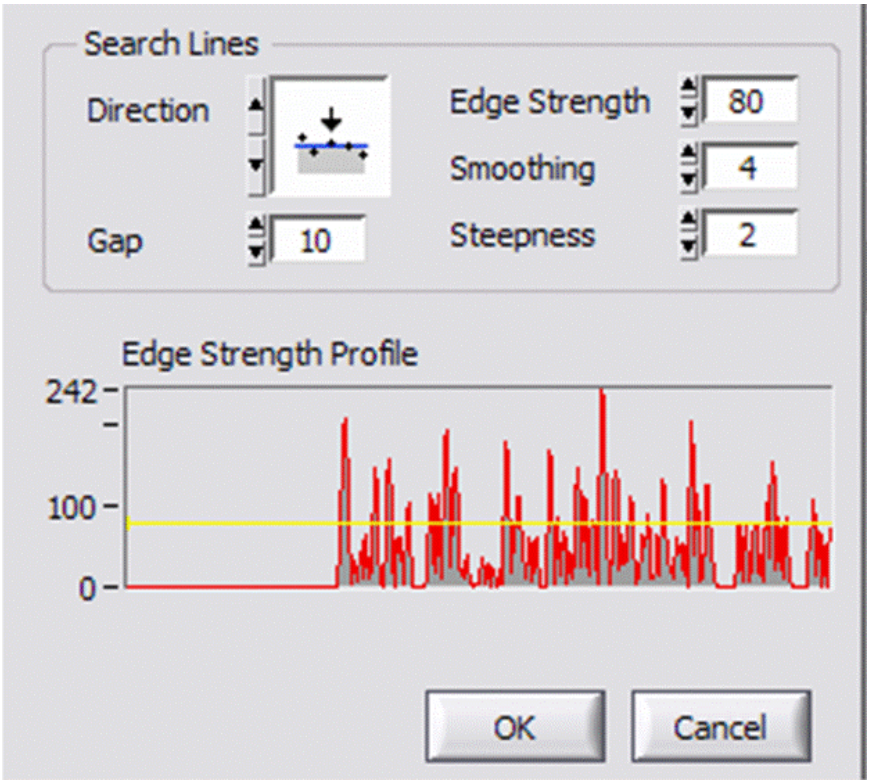


**Figure 24: Edge detector setup using NI Vision Assitant 7.1**

The edge detector required a region of interest and which direction it was to find a line. Four of the radiographs are shown in Figure 25.

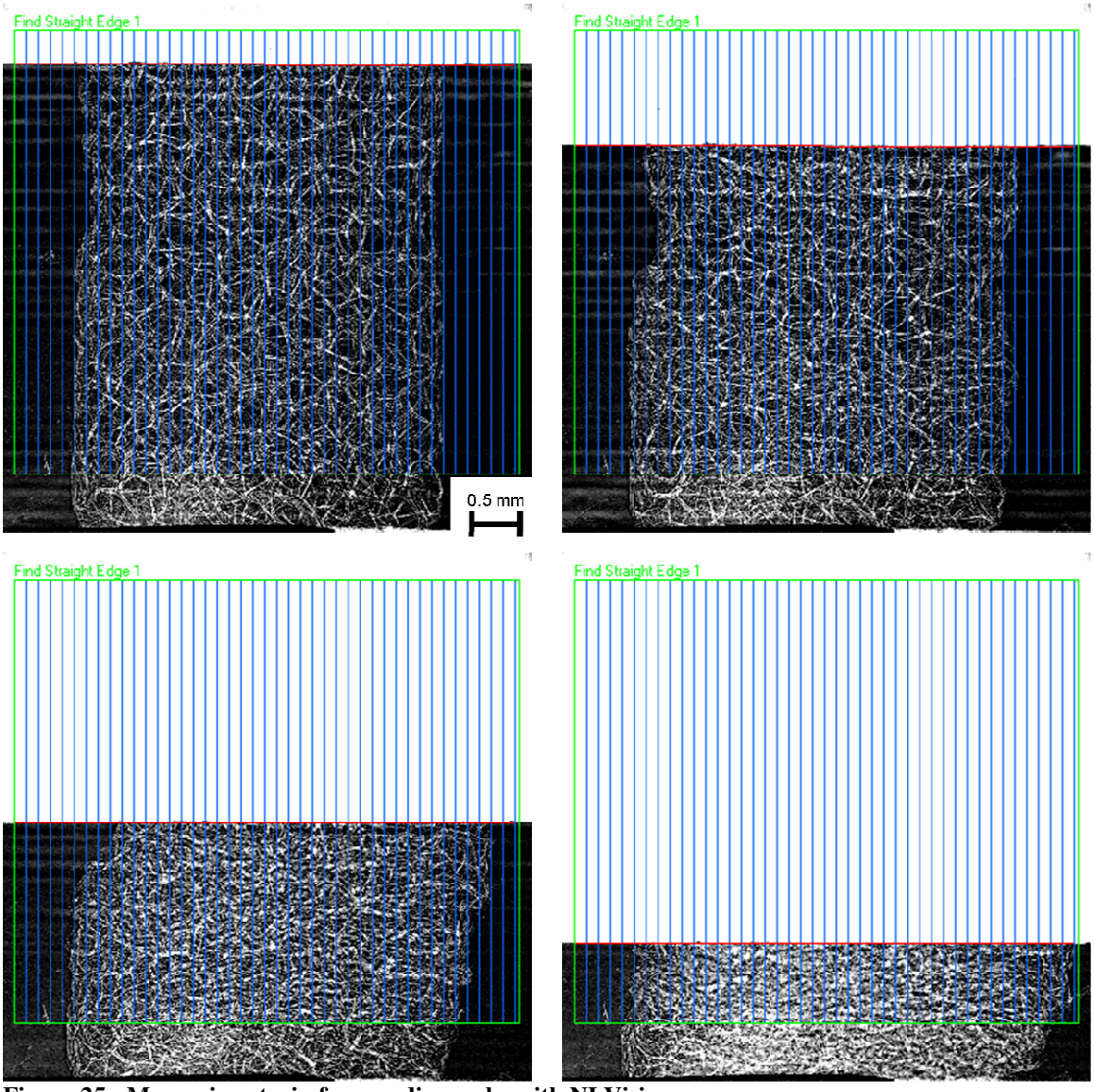


**Figure 25: Measuring strain from radiographs with NI Vision.**

The output from Vision Assistant consisted of a text file with coordinates for the each end of the line. An average was taken from these points and the strain was calculated according to equation 6.

$$\varepsilon = \frac{l_o - l}{l_o} \tag{6}$$

Where $l_o$ is the original gauge length determined by the distance from the line to the bottom of the image and $l$ is the instantaneous position of the line.

## 3.2 Tomographic imaging

The process of tomography is very similar to radiography. In fact, tomography uses radiographs which are taken as the sample is rotated in the X-ray beam. The setup used at Argonne National Lab is shown in Figure 26. The sample was rotated a total of 180° at quarter of a degree increments, where a radiograph was taken at each increment. The national lab had software that subtracted the background from each radiograph then used an algorithm which used all of the 720 radiographs to produce a representation of the sample [De Carlo *et al.* 2004].

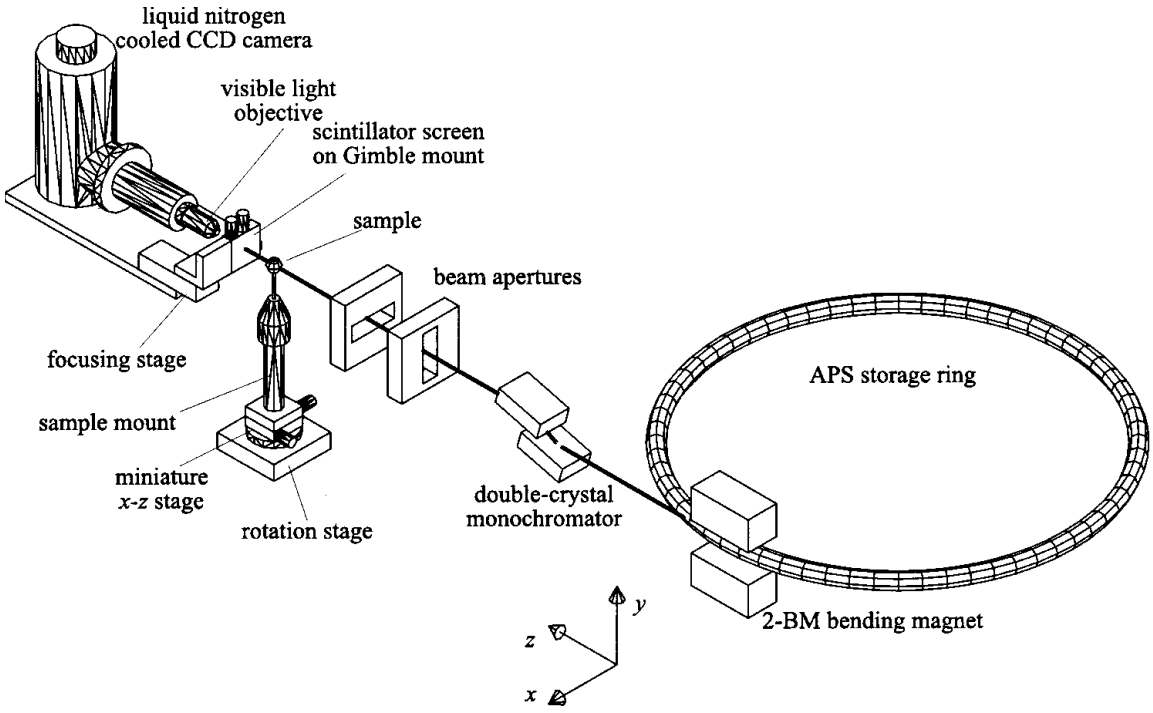


**Figure 26: Experimental setup at Advanced Photon Source. The monochromated beam is narrowed with the beam apertures then passed through the sample. A scintillator is used to transfer the X-rays to visible light, which is then focused onto the tomography CCD [Wang 2001].**

### 3.2.1 Tomography of a specimen under stress

One complication with tomography is keeping the sample still while taking radiographs. With the setup used, it took about three hours to perform a tomography scan. This time was longer than normal due to the sample contrast and the type of camera used. Each radiograph was 2048 x 2048 pixels across and some time was needed to store and move each frame between exposures. The system took 720 radiographs per tomography scan, and the exposure time for each radiograph was set to 12 seconds. The remainder of the 3 hour time span was spent saving the data from the previous scan and preparing for the next. Optimized scans can take as little as 15 minutes. Creep of the materials tester was a concern given the large amount of time needed for each scan. To reduce/eliminate the movement of the sample due to the creeping of the materials tester, a control program

was written to maintain constant stress. This proved to be efficient as there is no noticeable movement of the sample in the radiographs; however, using a load controlled approach is limits where tests can be stopped along in the stress strain curve. For example, it is impossible to maintain constant load at the peak yield stress. To maintain constant load, tomography was done in portions of the stress-strain curve where minima were observed. Positions of tomography scans are shown in Figure 27.

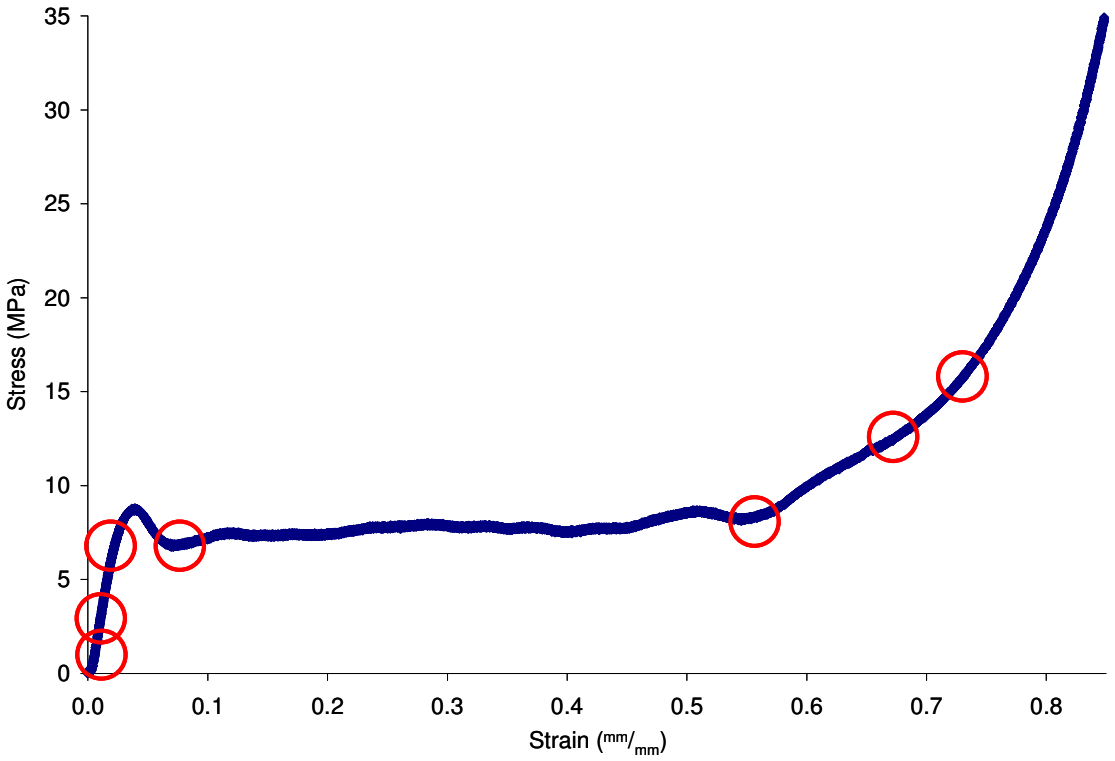


**Figure 27: Stress-strain graph of the PMI foam with the tomography data sets locations labeled by circles.**

### 3.2.2 Absorption vs. phase contrast

The experimental setup can be changed to emphasize absorption or phase contrast. This is done by changing the distance of the CCD (or other detector) from the sample. To

obtain the maximum ratio of absorption to phase contrast the sample should be placed as close to the detector as possible. This would provide mostly absorption contrast, but there would still be a negligible amount of phase contrast. The amount of phase contrast increases as the sample is moved away from the detector.

Phase contrast enhances edges and highlights features too small to be observed by absorption contrast. For example features such as cracks can be highlighted with phase contrast. To observe purely the phase component of the beam, an analyzer crystal or interferometer method is necessary [Hanan 2006]. Examination of phase contrast in detail is beyond the scope of this study.

Phase contrast was observed in this study by necessity of the experimental setup. A compound refractive lens was placed in the beamline for simultaneous diffraction measurements on other samples; however in order to use the 2048 x 2048 pixel camera the scintilator was limited to a distance of about 0.3 meters from the sample. This highlighted the edges of the samples as shown in figure Figure 28. Clearly the fringes associated with phase are observed. However, the reconstruction algorithm does not fully account for phase contrast. In addition the absorption of low-Z elements such as carbon found in PMI foam is low. Thus the experiment relies on post processing to clearly observe the foam micro-structure.

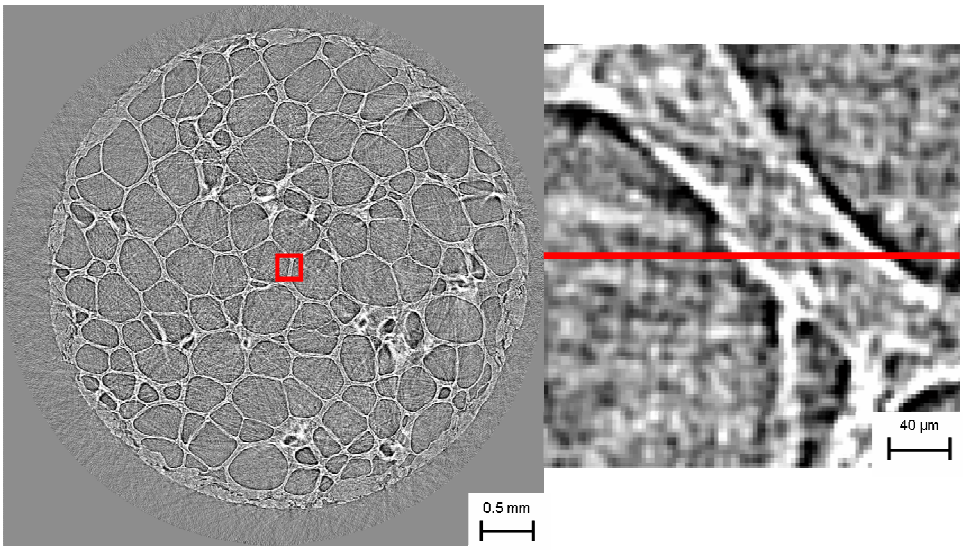


**Figure 28: Tomograph of the PMI foam with a zoomed in portion, which shows the edge enhancement due to phase contrast.**

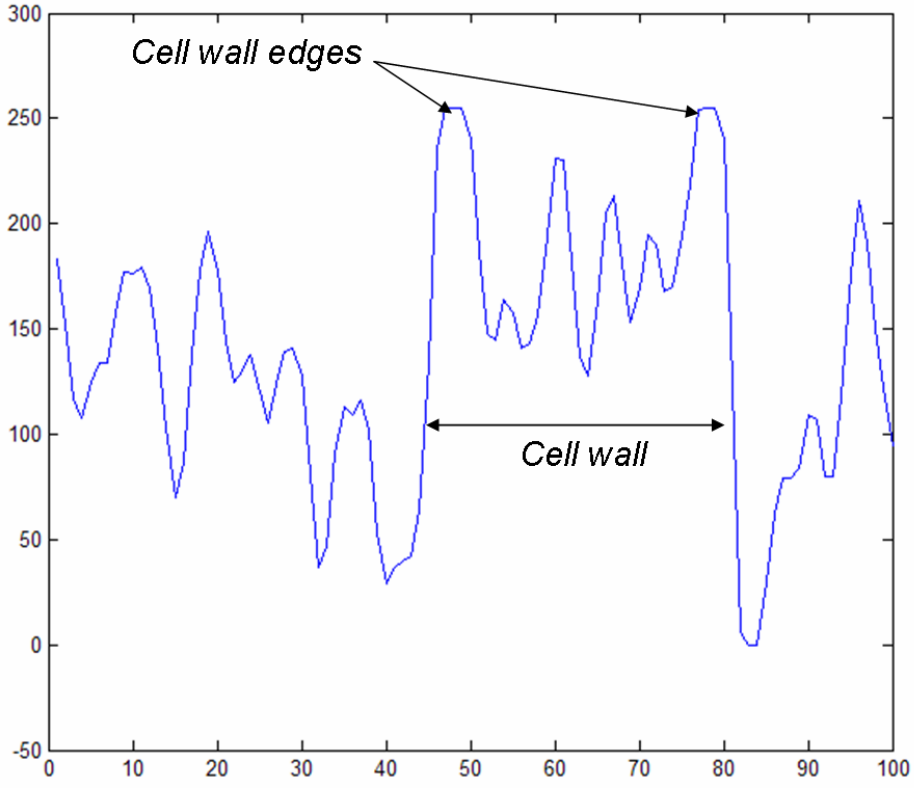


**Figure 29: A plot of the intensitys across the line shown on the zoomed in portion of Figure 28.**

### 3.2.3 Processing the tomographs for analysis

The BMG and polymer foams came from two different synchrotron facilities, which both stored the raw data differently. Despite the differences, the process involved to view the data is very similar. The raw data has to be converted to a compatible format such as TIFF, the histogram should be balanced to increase contrast without throwing away useful information, and lastly consideration for conversion for simulation in GIMP.

The European Synchrotron Radiation Facility system divided the BMG foam sample into upper and lower halves in order to accommodate the large file size. This method requires that the halves be shifted along the x and y axes to align them. This tedious process was done by hand once the files hade been converted and saved as TIFF images.

#### 3.2.3.1 Opening and handling the raw data

The BMG foam was inputted into Amira which was then used to convert the data to TIFF.

1. opened stck file
    a. had to know the dimensions and header size
    b. match requested file size with actual file size
2. balanced the histogram
3. saved as a series of 2D tiffs
4. aligned top and bottom halves
5. converted to material points
6. applied a cutoff on the low end until the density was correct

The polymer foam has phase contrast which requires some extra processing. The raw data is stored as a set of Hierarchical Data Format (HDF) files, each of which includes a floating point array. Each file is about 12 megabytes in size and the sets of data had 1792 files per set, which is slightly larger than 20 gigabytes per set. Even if the tomography files had been free of noise and phase contrast the data would still be to large to directly load into 3-dimensional visualization software. The data was converted to 8-bit images using a program written in MatLab. The respective 8-bit images are about 4 megabytes each and 7 gigabytes per set, which is a 66% reduction in file size from the original HDF file.

#### 3.2.3.2 Balancing the histogram

The apparent contrast of the images as viewed on a monitor or print can be drastically increased by balancing the histogram of the image. In reality, no information is added to the image, only the way it is displayed is altered for clarity. Once saved to 8-bit information outside the retained dynamic range is lost, but this information can always be reintroduced from the original files. A sample histogram from one of the polymer foam images before it was balanced is shown in Figure 30. The x-axis for the histogram is the intensity of the pixel values from the picture, and the y-axis is the frequency (number of occurrences) for each frequency. The gray scale for 8-bit images ranges from 0 (black) to 255 (white). The largest value in this histogram is 17, so the image looks completely black.

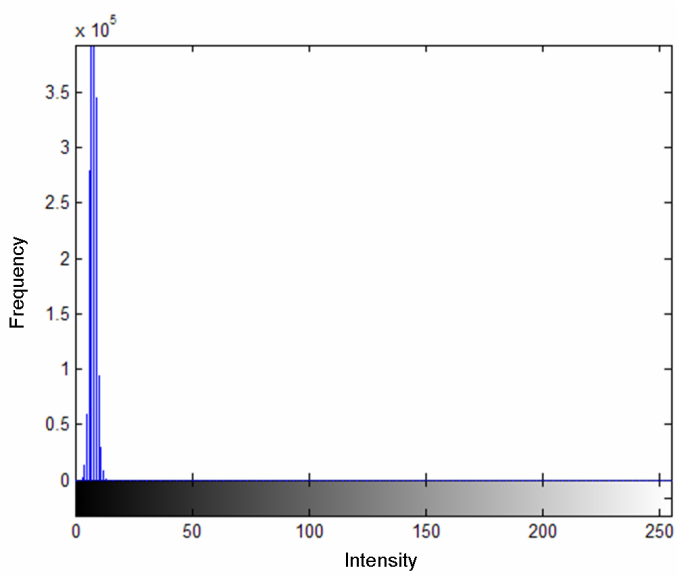


**Figure 30: The histogram from one of the polymer foam images before it was balanced. The gray scale color bar is shown at the bottom of the histogram.**

The concept of balancing the histogram is to expand the intensity values so that they cover the entire range of gray scale values. The balanced histogram and its resulting image are shown in Figure 31. The foam sample in the image is now visible since the intensity values cover the entire range of gray scale values. Some information is lost in truncating the tails of the histogram.

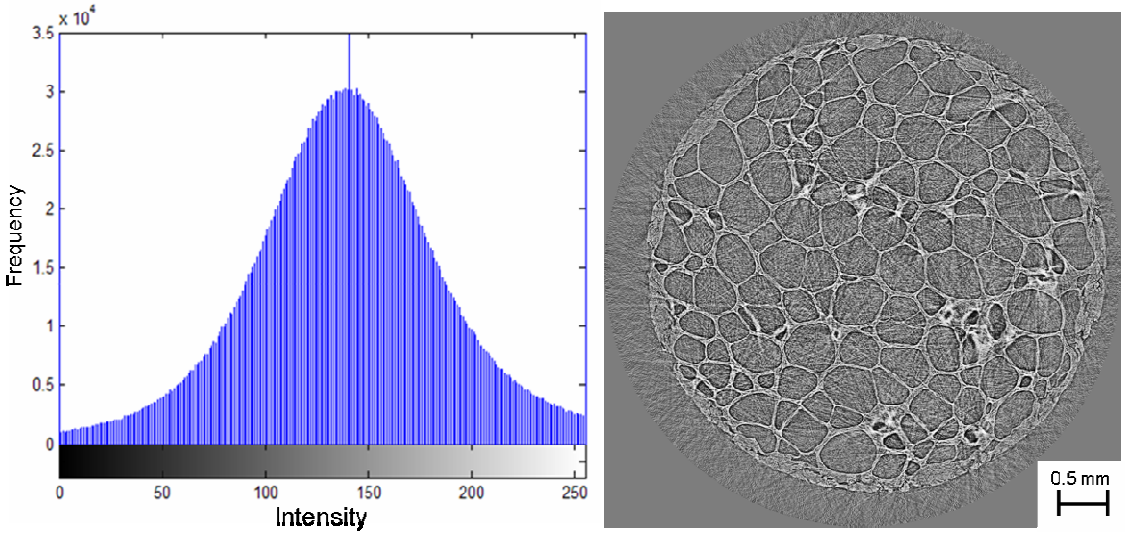


**Figure 31: The balanced histogram of the polymer foam and the resulting image. 0 corresponds to 0 in the original image and 255 corresponds to 17. Phase contrast leads to streaking in the reconstruction.**

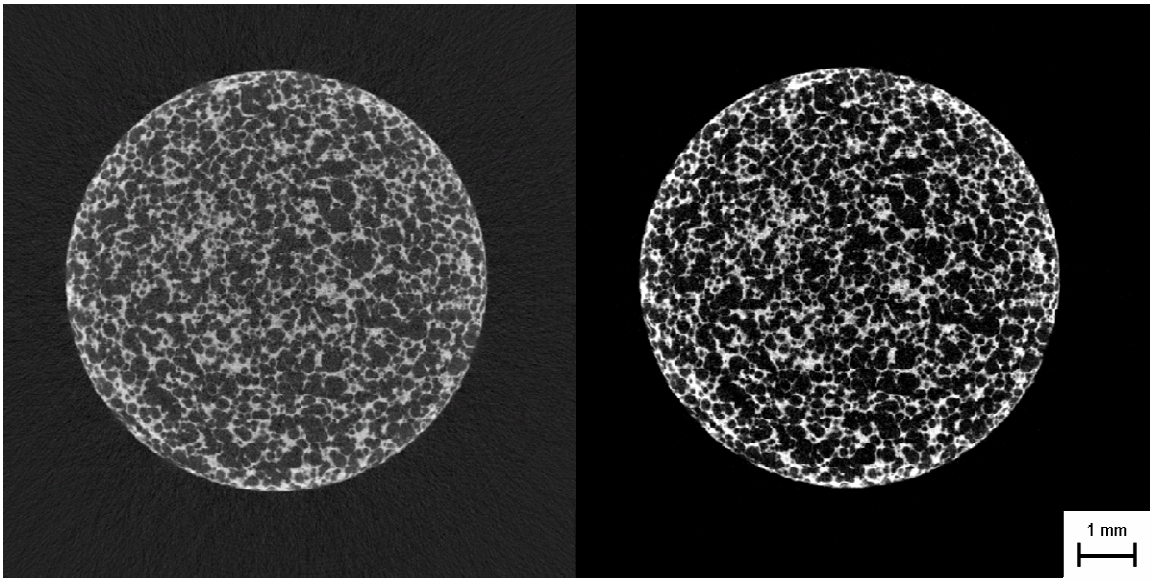


**Figure 32: Before and after images of the BMG foam from balancing the histogram.**

All of the shown images and histograms are 8-bit. It is important to note that the histograms were balanced before the images were converted to 8-bit. The raw data is floating point and has about 12 decimal places for every pixel's intensity value.

### 3.2.3.3 Filtering noise from reconstructed images

As in Figure 31, the main structure of the polymer foam is visible, but there is noise inside the cells which causes problems when reconstructing a 3-dimension model. After initial examination of the image the noise seemed to consist of high frequencies, while the foam cell walls occur at a much lower frequency. This type of problem can typically solved by filtering in the Fourier domain. In the Fourier domain the lower frequencies occur in the center of the image and the frequency increases to the edge of the image. The Fast Fourier Transform (FFT) approximates the Fourier Transform by truncating higher order terms. The FFT of the histogram balanced image is shown in Figure 33.

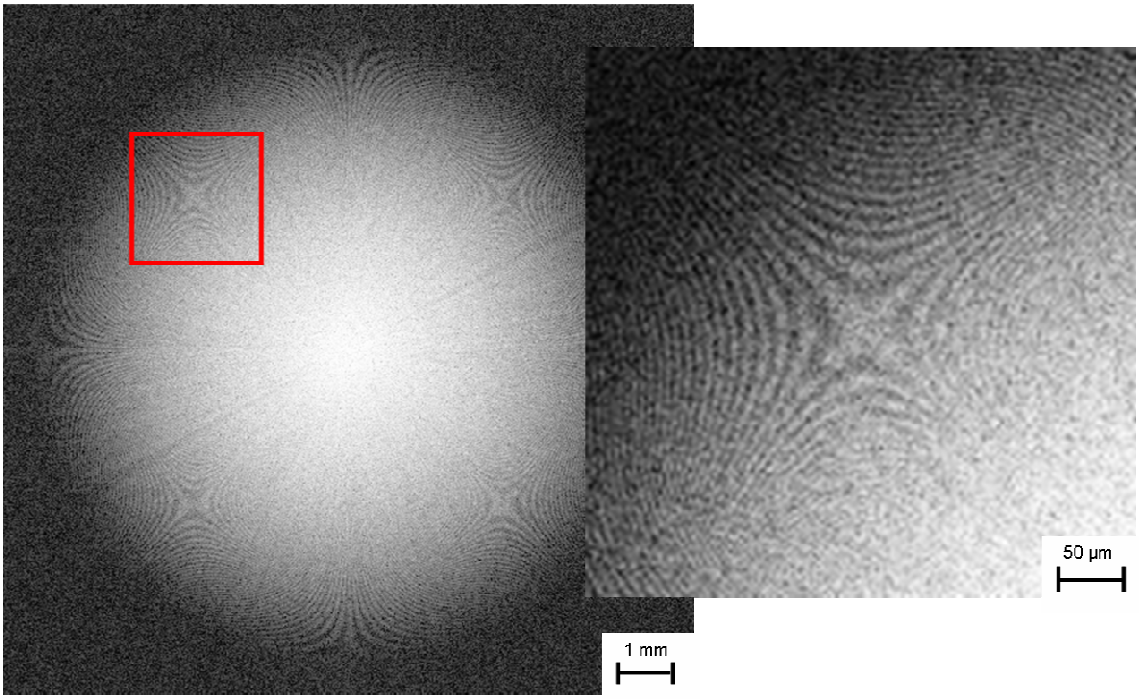


**Figure 33: Fast Fourier Transform of the original image before the histogram was balanced. The zoomed in portion is outlined with the red box.**

A simple low or high band pass filter can be made by blocking different regions of the FFT by means of setting the pixels values to zero (black). After the FFT is modified the image must be converted back to the spatial domain by taking the Inverse of the Fast Fourier Transform (IFFT). During the conversion to the spatial domain, any frequency values that were set to zero in the FFT are then converted to zero (black) in the spatial domain. The next two sets of images demonstrate the effects of blocking a center (high-pass) and outer (low-pass) portion of the FFT image. In the first set the area around the sample became black after taking the IFFT because it consisted of low frequencies.

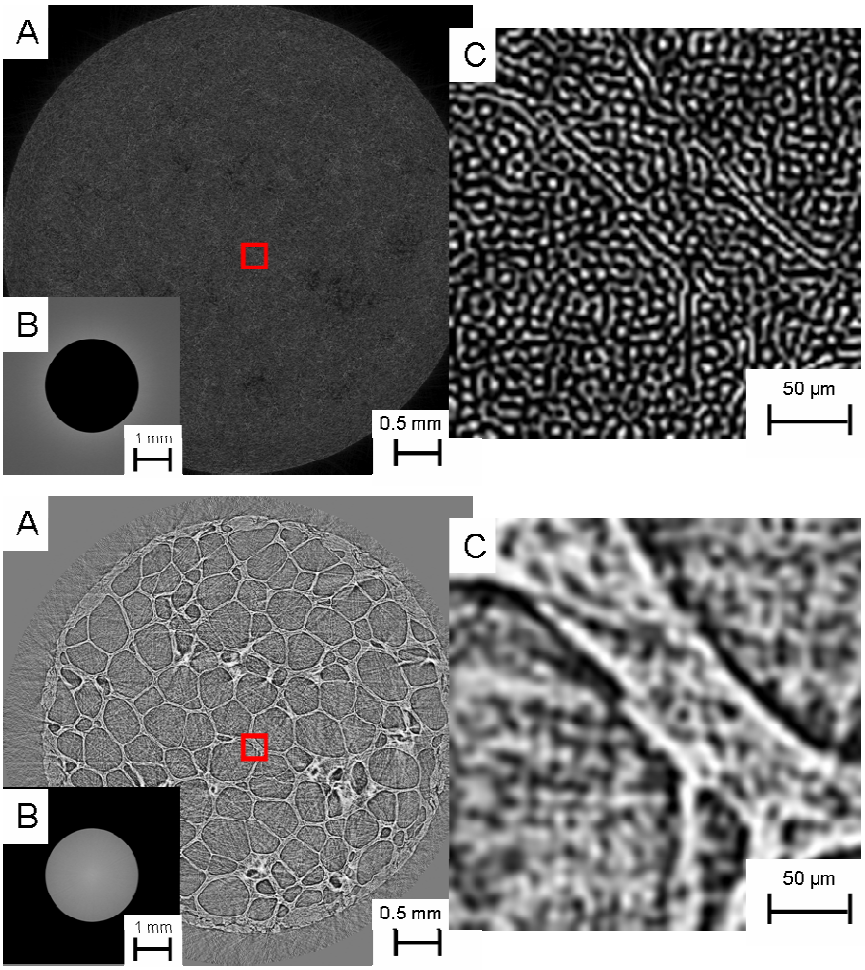


**Figure 34: Each set of images contain a filtered tomograph of the polymer foam (A), the corresponding filtered Fourier Transform (B), and a close-up view of a cell wall (C).**

The previous images served as a basic example. The next four pairs demonstrate the effects of lowering the cutoff value for blocking the high frequencies. This was hypothesized as a solution for the reduction or possibly even elimination of the noise in the images.

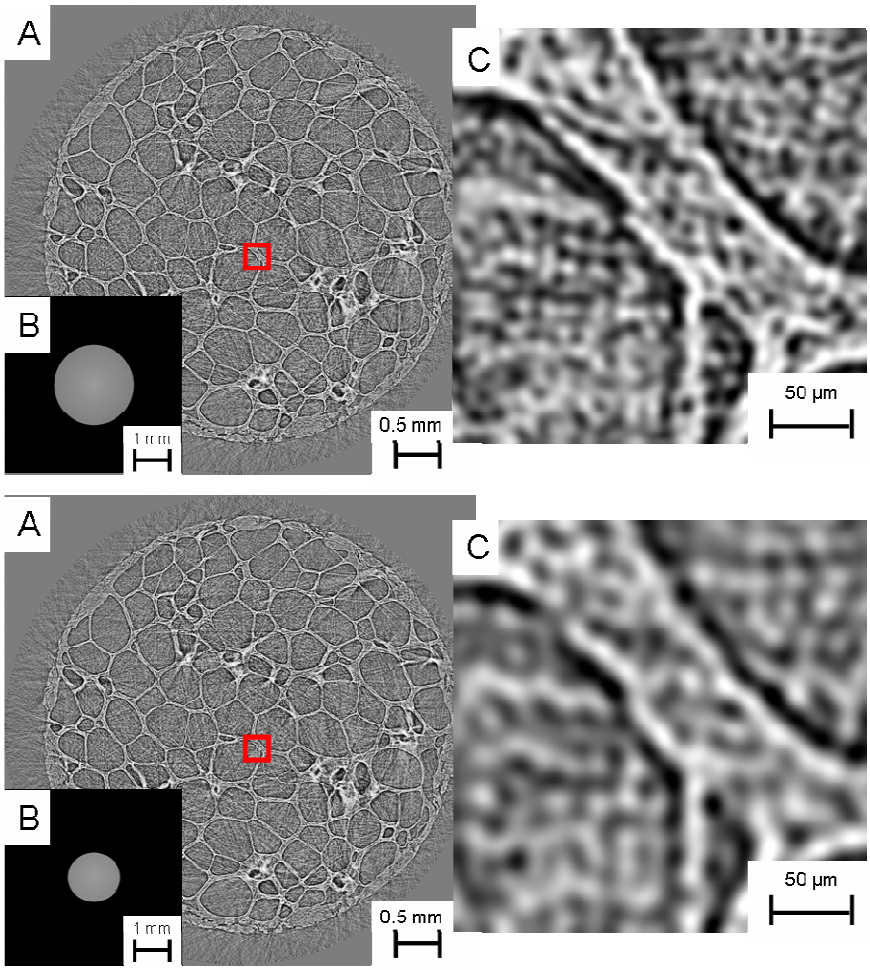


**Figure 35: Each set of images contain a filtered tomograph of the polymer foam (A), the corresponding filtered Fourier Transform (B), and a close-up view of a cell wall (C).**

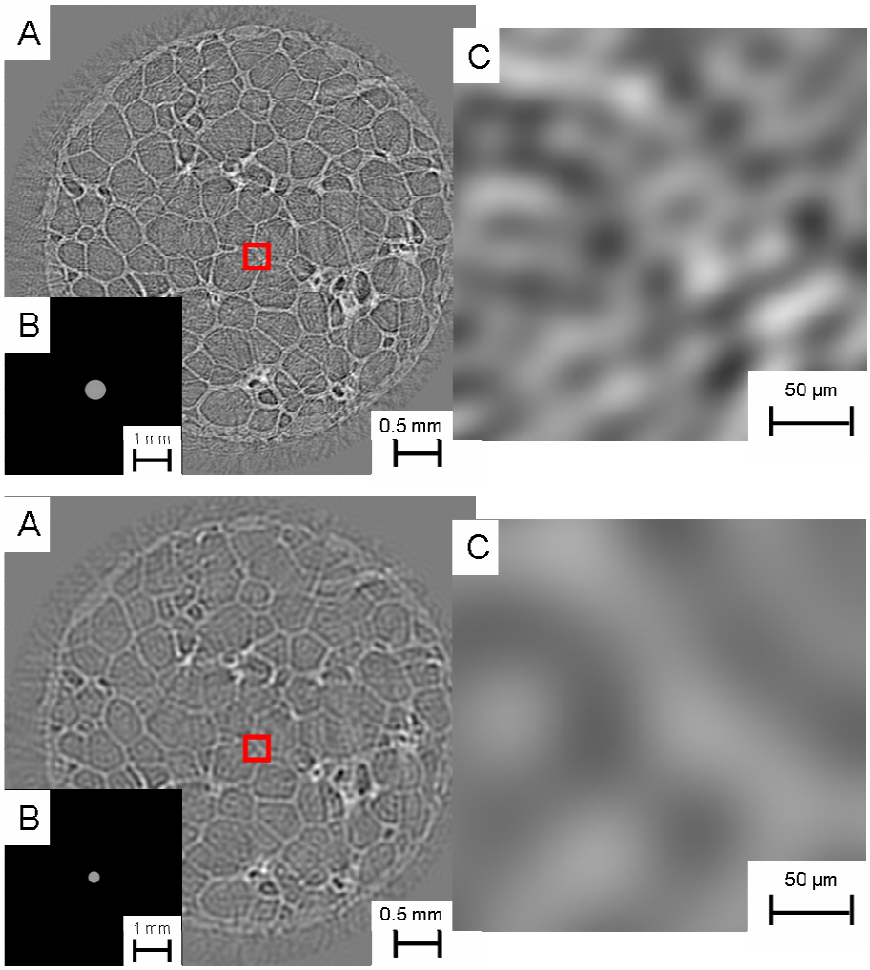


**Figure 36: Each set of images contain a filtered tomograph of the polymer foam (A), the corresponding filtered Fourier Transform (B), and a close-up view of a cell wall (C).**

Through these examples it is evident that the simple low-pass filters do not perform as well as desired on these tomographs. There are some minor changes between the data sets, but there is not a significant change in the resulting image until the last set shown. Reducing the frequency cutoff to the extent of the last data set resulted in a blurred image where the walls are becoming less clear.

The material of the cell walls consists of the same high frequency noise as the cells. This is why removing the high frequency intensities starts eroding the cell walls as the cutoff

frequency is lowered. This can be a problem with phase contrast, which is typically used to enhance the edges in the sample [Davis 1995].

There has been some promising work done on filtering out the noise of data that has phase-contrast [Youssef *et al.* 2005]. In Youssef's work, there are six image processing steps which are undergone to yield a data set that is ready for a finite element method.

#### 3.2.3.4 Reducing the data for analysis via the Generalized Interpolation Material Point Method (GIMP)

Each original set of raw data for the polymer foam is a little over 20 GB, which is large enough to create problems in producing a 3-dimensional visualization of the sample, but for 3-dimensional modeling, the size of the data is a greater concern due to computational time. Therefore, the data was not only reduced in size by changing it to 1-bit, but also by reducing the resolution. All of these were done with a program written in Matlab as shown in the appendix.

### 3.2.4 Damage assessment

The initial collapse in foams is generally located along a certain plane. It is obvious where the plane is when a slice along the z-axis is taken from the data set from before failure and after failure, and then they are subtracted from each other. This method is very effective since the failure occurs along a single plane and the portion above or below the plane remains similar.

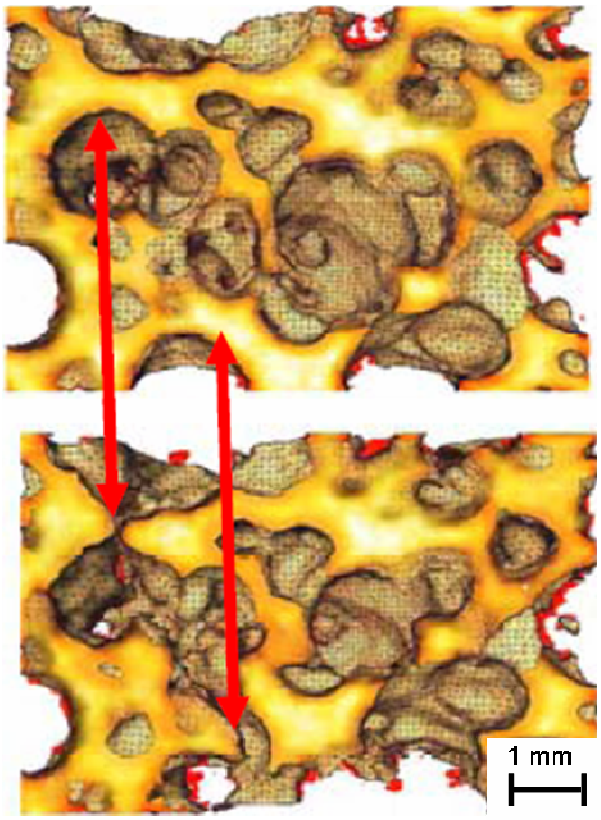


**Figure 37: Local brittle failures in the bulk metallic glass foam shown via a 3-dimensionally rendered image from a tomograph.**

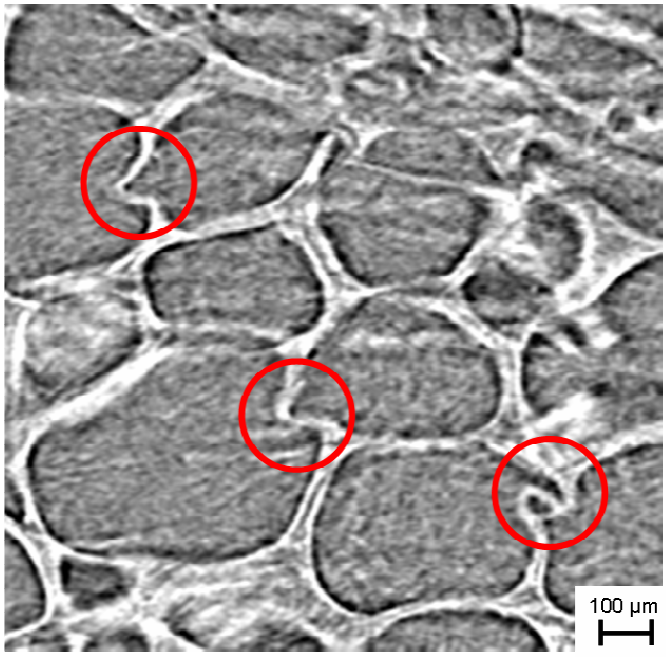


**Figure 38: Local plastic failures in the polymer foam.**

### 3.2.5 Measuring two-dimensional strain

To measure the strain from the tomographs, a slice had to be taken from along the z-axis of the data sets. This is fairly simple process, since the original images are on the x-y plane. A program was written in Matlab which opened each image and stored a row of data from each image and placed it into a new image creating a slice in the x-z plane.

Two dimensional strains have been too hard to determine via radiographs; however, with tomography it is much easier. Measuring two-dimensional strains in a foamed sample involves finding a landmark, such as a cell, cell wall, or cell edge, which can then be tracked throughout the deformation of the sample. Such landmarks are hard to find and follow with radiographs as can be seen in Figure 39.

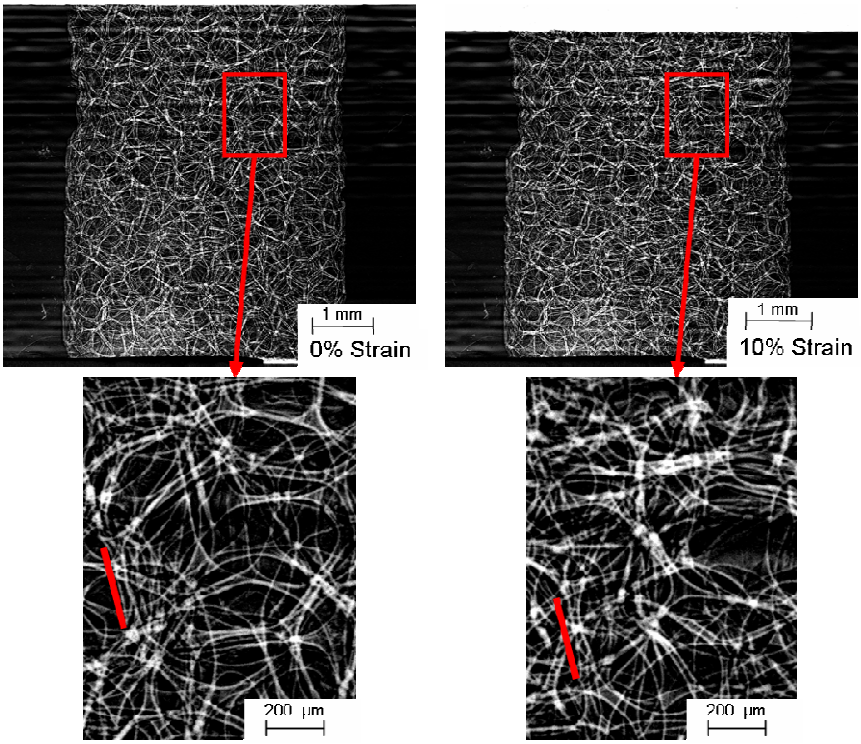


**Figure 39: Radiographs at 0 and 10% strain of the polymer foam, showing the difficulty in measuring strain in two dimensions without a clear landmark to follow.**

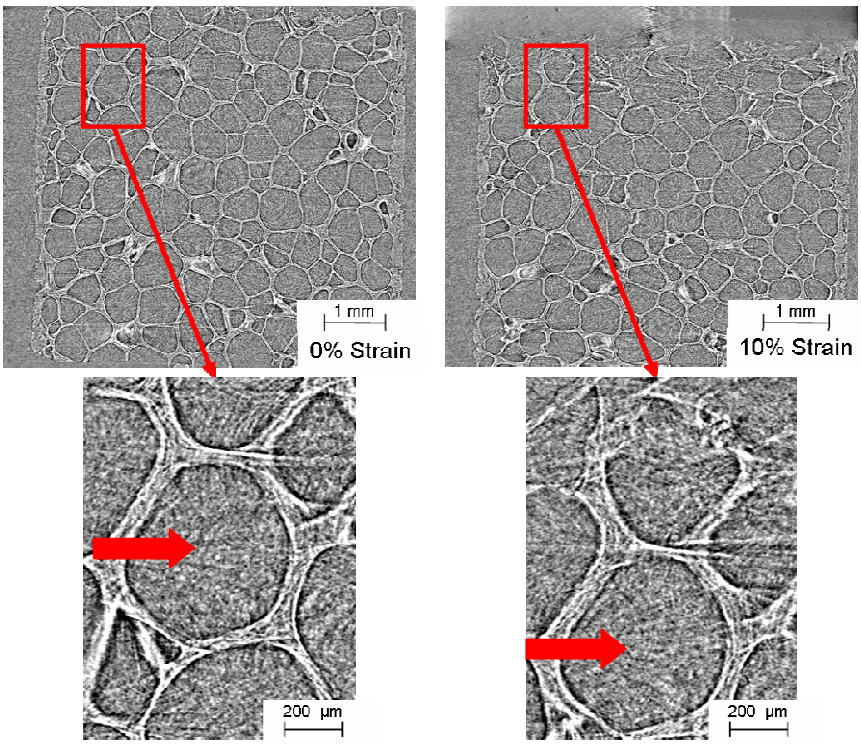


**Figure 40: Tomographs at 0 and 10% strain of the polymer foam. A cell is marked with the red arrow to demonstrate the effectiveness of measuring strains in 2-dimensions with tomographs.**

In the tomographs, certain cells, groups of cells, and ligaments can be picked to determine local strains. This can be done by following the region of interest by hand or by a pattern matching program. The pattern matching tool in NI Vision Assistant was used in effort to calculate the strains from the radiographs of the polymer. The large amount of changes in the radiographs only enabled the software to accurately detect the region up to 10% strain. Measuring the strain from the radiographs was also tried by hand, which was only successful to 12% strain. The complication in following certain landmarks in radiographs comes from the randomly placed cells in the foamed samples. The variations in the cell placement, cell size, cell wall size, and cell edge size all play a role in the location of the deformation plane caused by the initial collapse. Due to these factors, the deformation plane does not occur along a linear plane, but rather a random

curved shape. The deformation plane from the BMG foam in shown in Figure 41: where the plane is outlined by the red line.

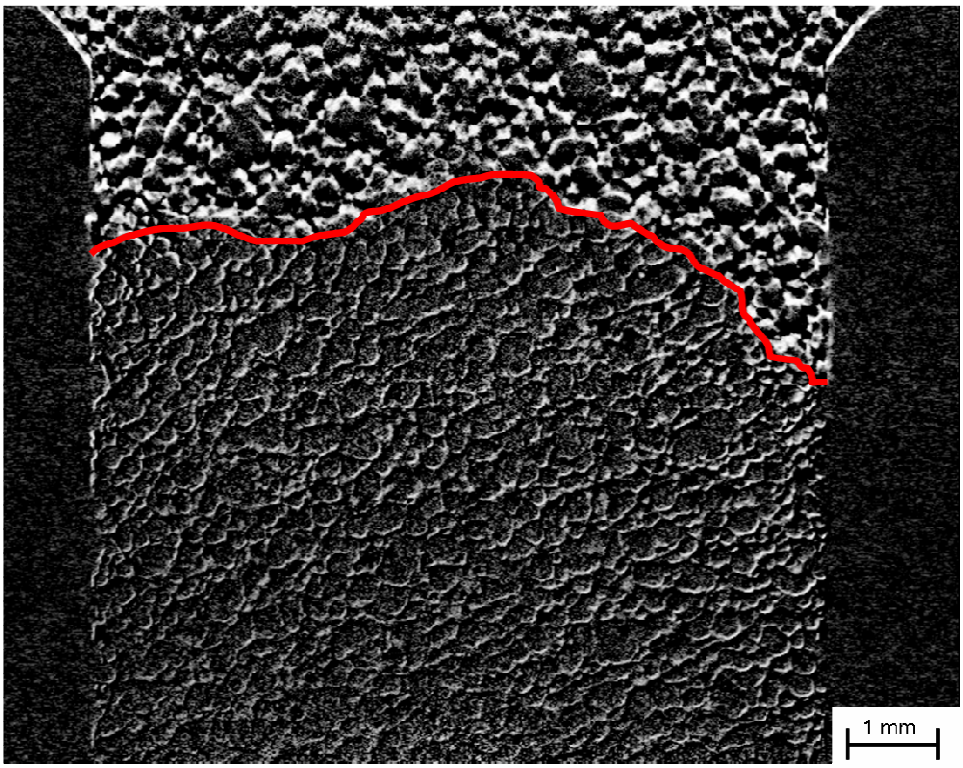


**Figure 41: The deformation plane from the bulk metallic glass specimen.**

The curvature of the deformation plane makes tracking the strains 2-dimensionally very hard in radiographs. Three close-ups of radiographs taken from the polymer foam are shown in Figure 42.

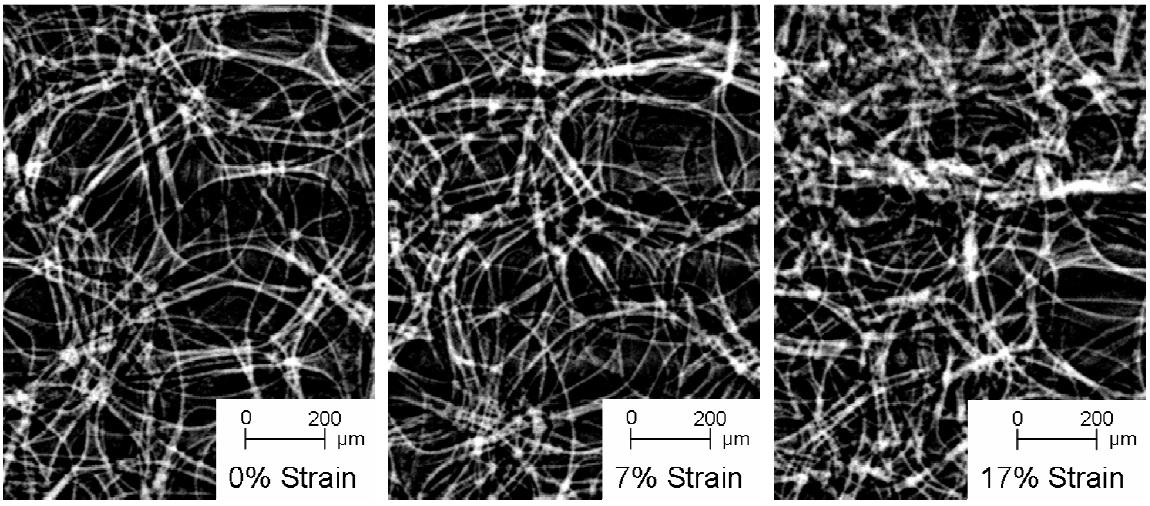


**Figure 42: Close-ups of radiographs from the polymer foam. These images demonstrate the difficulty in determining 2-dimensional strains with radiographs.**

## 3.3 Modeling and validation of stress predictions

To date there have been several methods used to determine the response of foamed specimens. The Finite Element Method (FEM) has been used by Wicklein [Wicklein 2005] to determine the behavior of aluminum open-celled foam specimens in the elastic region. Youssef [Youssef *et al.* 2005] investigated the response of a polyurethane foam to a compressive strain of 20% using a finite element method. Analytical models have been developed by Gibson and Ashby [Gibson and Ashby 1997] which predict the elastic, plastic plateau, and densification regions. More recent work using the Generalized Interpolation Material Point Method (GIMP) [Ma, 2007] has shown a promising output for compressive strains into the densification regime. For the purpose of this paper only the analytical and the GIMP will be discussed.

### 3.3.1 Analytical models

There are three deformation regimes in foams: the elastic region, plateau region, and the densification region [Gibson and Ashby 1997 Ch. 5]. The equation used to predict the elastic modulus of the polymer foam is shown in equation 7. Where $\varphi$ is the fraction of the solid in the faces vs. the edges, $\rho^*/\rho_S$ is the relative density (density of the foam divided by the density of the parent material, $p_o$ is the internal pressure inside the cells (when introduced in the processing method), $v^*$ is the Poisson's ratio, $E^*$ is the elastic modulus of the foam, $E_S$ is the elastic modulus of the parent material in solid form.

$$E^* = \varphi^2\left(\frac{\rho^*}{\rho_S}\right)^2 + (1-\varphi)\left(\frac{\rho^*}{\rho_S}\right) + \frac{p_o(1-2\nu^*)}{E_S(1-\rho^*/\rho_S)} \tag{7}$$

The last term in equation 7 accounts for the internal pressure in the cells. When the internal pressure term is considered; the resulting modulus changes by less than 0.01% compared to when it is neglected. The relative density of both foams was determined by dividing the mass by the volume. The volume of the metal foam was available by Archimedes method where the volume of the PMI foam was available by measuring the sample dimensions. To determine the elastic modulus of the parent material, nanoindentation was performed on thick cell walls and the average was taken from several tests [Daphalapurkar *et al.* 2007]. The graph from nanoindentation for the polymer sample is shown in Figure 43. This plot shows the relaxation modulus with respect to time, which shows that for slower strain rates the elastic modulus of the polymer is 3.73 GPa. This value seems slightly lower than the values for similar

polymers; however, due to the viscoelastic behavior of this material and the given strain rates, this value is consistent with other polymers in its family.[Matweb 2007] The modulus for the bulk metallic glass was found using the same technique.[Ma 2006]

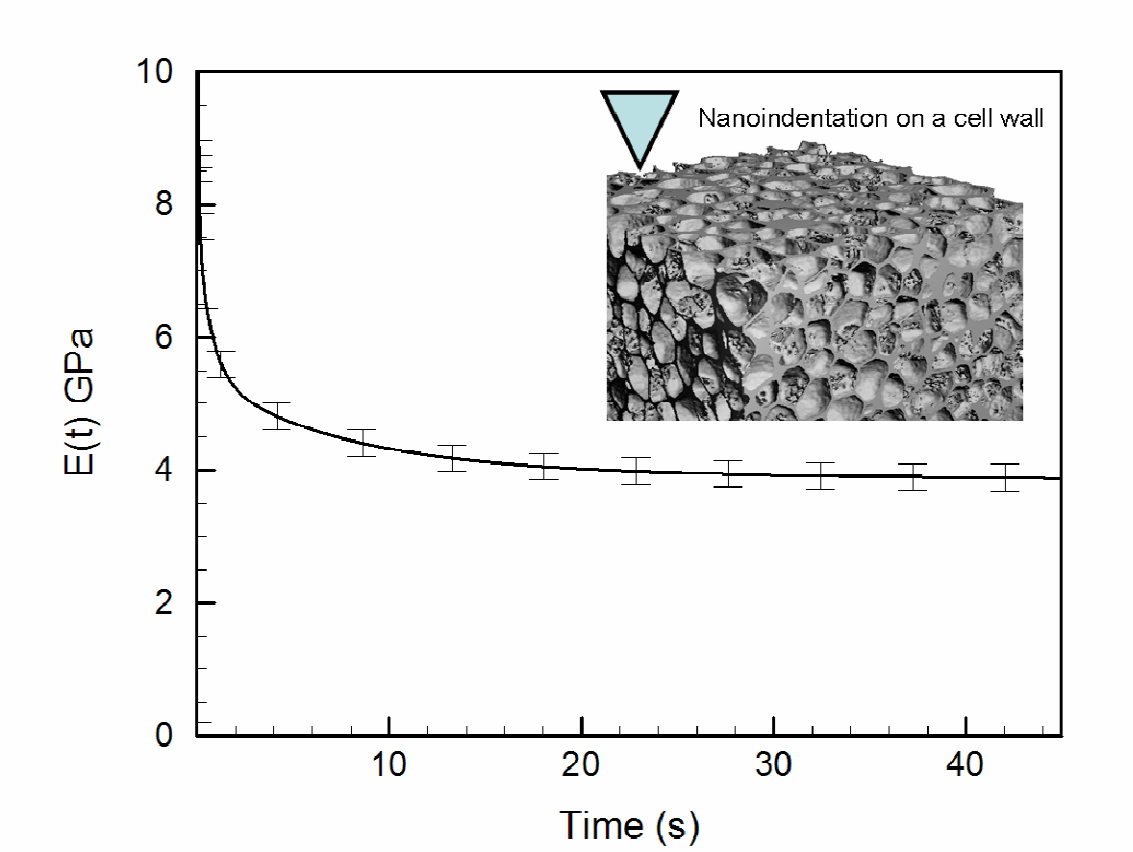


**Figure 43: Elastic modulus versus time from the nanoindentation of a thick cell wall on the polymer foam. The inset illustrates nanoindentation being performed on a cell wall of the polymer foam, which has an average cell size of 0.3 mm. [Daphalapurkar *et al.* 2007]**

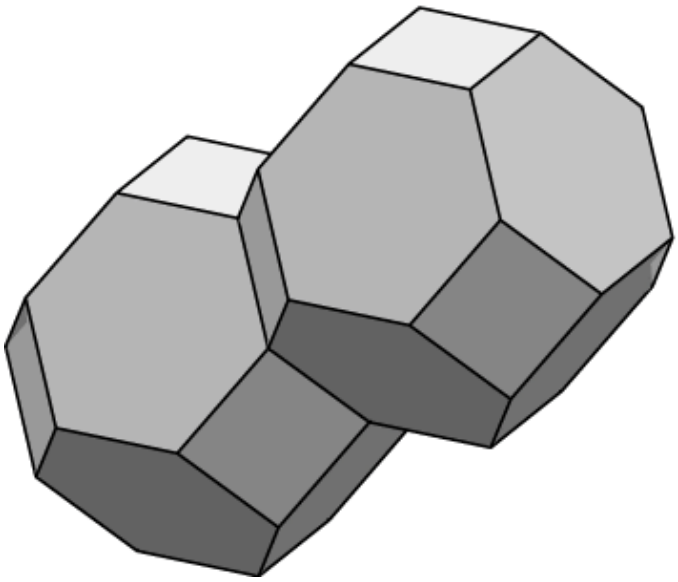

**Figure 44: Geometry of the tetrakaidecahedral cell.**

The parameter, $\varphi$ (the volume fraction of solid in the cell edges), can be hard to determine since the cells are randomly placed and vary in size and shape. To calculate the ratio, $\varphi$, one much first decide the proper geometry equations to use. For approximating the polymer and bulk metallic glass foams, the equations for the tetrakaidecahedral cell geometry were used (see Figure 44). This geometry, which determines two of the parameters for the ratio, $\varphi$, was chosen based on the edge and face connectivity of the foamed specimen. The edge ($Z_e$) and face connectivity ($Z_f$) are the number of edges that meet at a vertex and the number of faces that meet at an edge, respectively. For the tetrakaidecahedral cell, $Z_e = 4$ and $Z_f = 3$. Measurements from tomographs were taken from the sample to determine the last three variables: the thickness of the cell faces ($t_f$), the thickness of the cell edges ($t_e$), and the length of the cell edges ($l$). The relationship between these three variables and the microstructural geometry to determine the ratio ($\varphi$) is shown in equation 8

$$\varphi = \frac{t_e^2}{t_e^2 + \frac{Z_f}{n} * t_f * l} \tag{8}$$

This ratio was determined for both the BMG and polymer foams. It is difficult to determine an accurate value for the variables used to calculate $\varphi$; which is critical since the equations for the foams elastic modulus and the plateau stress are greatly influenced by its value. The experimental elastic modulus was calculated from two sets of points taken from the experimental curve shown in Figure 45. Two different elastic moduli lines are shown in Figure 45. The value of 329 MPa was found from the experimental data while the value of 831 MPa was calculated from equation 7. The difference between the two moduli comes from the calculated volume fraction of cell edges; which is only used in calculations for closed-cell foams. This process was also performed for the bulk metallic glass foam. The predicted modulus for the BMG foam was calculated using the closed cell equation to be 9.1 GPa and the plateau stress was determined to be 133.7 GPa. The % difference for these values is 284% and 571%, respectively, for comparisons see Table below.

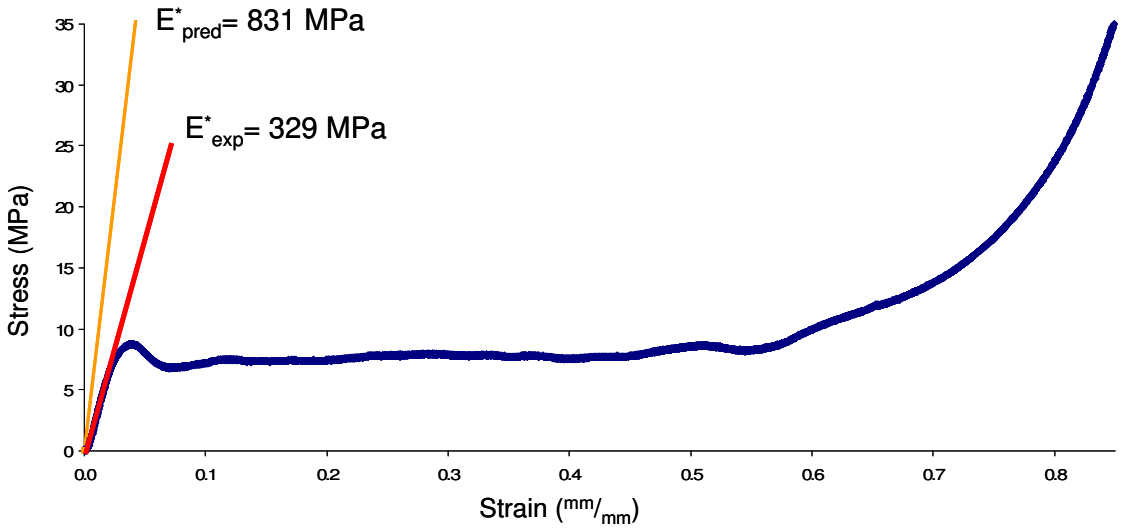


**Figure 45: General stress-strain curve of the polymer foam with the predicted elastic modulus ($E^*_{pred}$) and the one determined experimentally ($E^*_{exp}$).**

The plateau stress was calculated using equation 9; which also contains the relative density ($\rho^*/\rho_S$), the internal pressure of the cells ($p_o$), and the ratio of the cell faces to edges ($\varphi$) as in equation 7. The other terms in the equation include ($p_{at}$) the atmospheric pressure, ($\sigma^*_{pl}$) the plateau stress, and ($\sigma_{ys}$) the yield strength of the parent material. The equation for the plateau stress of brittle foams is very similar to that of the equation used for the polymer foam; however, it does not contain a term for internal pressure. Equation 10 shows the relationship for the plateau stress of brittle foams.

$$\sigma^*_{pl} = \sigma_{ys}\left[0.3\left(\varphi\frac{\rho^*}{\rho_S}\right)^{3/2} + 0.4(1-\varphi)\left(\frac{\rho^*}{\rho_S}\right) + \frac{p_o - p_{at}}{\sigma_{ys}}\right] \quad (9)$$

$$\sigma^*_{cr} = \sigma_{fs}\left[0.2\left(\varphi\frac{\rho^*}{\rho_S}\right)^{3/2} + 0.4(1-\varphi)\left(\frac{\rho^*}{\rho_S}\right)\right] \quad (10)$$

As the foam sample is compressed the cells inevitably collapse and the relative density increases. The point where the cells begin to completely collapse is determined by the initial relative density and not the material properties. The relationship between the beginning of the foams densification and its initial relative density is shown in equation 11. This equation can be applied to either elastomeric, elastic-plastic, or elastic-brittle foams since it is only dependent on the relative density.

$$\varepsilon_D = 1 - 1.4\left(\frac{\rho^*}{\rho_S}\right) \tag{11}$$

The material properties for both the bulk metallic glass and polymer foams are shown in Table 2, and the experimental and predicted values for both are listed in Table 3.

**Table 2: Material property values used for the predictions of the BMG and polymer foams.**

| | Bulk metallic glass (Brittle) | Polymer (Elastic-plastic) |
|---|---|---|
| Solid elastic modulus (GPa) | 108 | 3.73 |
| Relative density (%) | 17 | 30 |
| Face connectivity ($Z_f$) | 3 | 3 |
| Cell edge thickness ($t_e$) (mm) | 0.268 | 0.0521 |
| Cell edge length (l) (mm) | 1 | 0.267 |
| Cell face thickness ($t_f$) (mm) | 0.1 | 0.0447 |

**Table 3: Experimental and predicted values for the BMG and polymer foams.**

| | Elastic modulus | | |
|---|---|---|---|
| | Experimental | Closed cell prediction | Open cell prediction |
| **Bulk metallic glass (Brittle)** | 3.2 (GPa) | 9.1 (GPa) | 3.1 (GPa) |
| | | | |
| **Polymer (Elastic-plastic)** | 329.3 (MPa) | 831.0 (MPa) | 335.7 (MPa) |

| | Plateau stress | | |
|---|---|---|---|
| | Experimental (MPa) | Closed cell prediction (MPa) | Open cell prediction (MPa) |
| **Bulk metallic glass (Brittle)** | 24 ± 0.5 | 133.7 | 22.9 |
| | | | |
| **Polymer (Elastic-plastic)** | 7.7 ± 0.1 | 10.8 | 6.7 |

| | Densification | |
|---|---|---|
| | Experimental (%) | Prediction (%) |
| **Bulk metallic glass (Brittle)** | Not Available | 76.2 |
| | | |
| **Polymer (Elastic-plastic)** | 59 | 58 |

### 3.3.2 Generalized Interpolation Material Point Method

**The Finite Element Method (FEM)**

Despite the success of FEM it is less accurate when predicting large strains. This is due to its grid which moves with the sample. Recently, in 1999, the Material Point Method (MPM) was introduced which used a stationary grid where the properties of the specimen were calculated at the nodes.

The stress-strain curve of the BMG foam microstructure simulated with GIMP has a very smooth curve as the strain increases, as shown in Figure 46. This is due to the plastic yield simulated for the material points. However, this is not typical of BMG which acts as a brittle foam at porosities near 70%. The experimental curve shown in Figure 47 is an

example of the typical stress plateau in brittle foams. The plateau region is begins with a sharp failure at the peak of the specimen's elastic region followed by jagged edges all along the plateau region. In many cases, the brittle foam spalls so that densification is not observed.

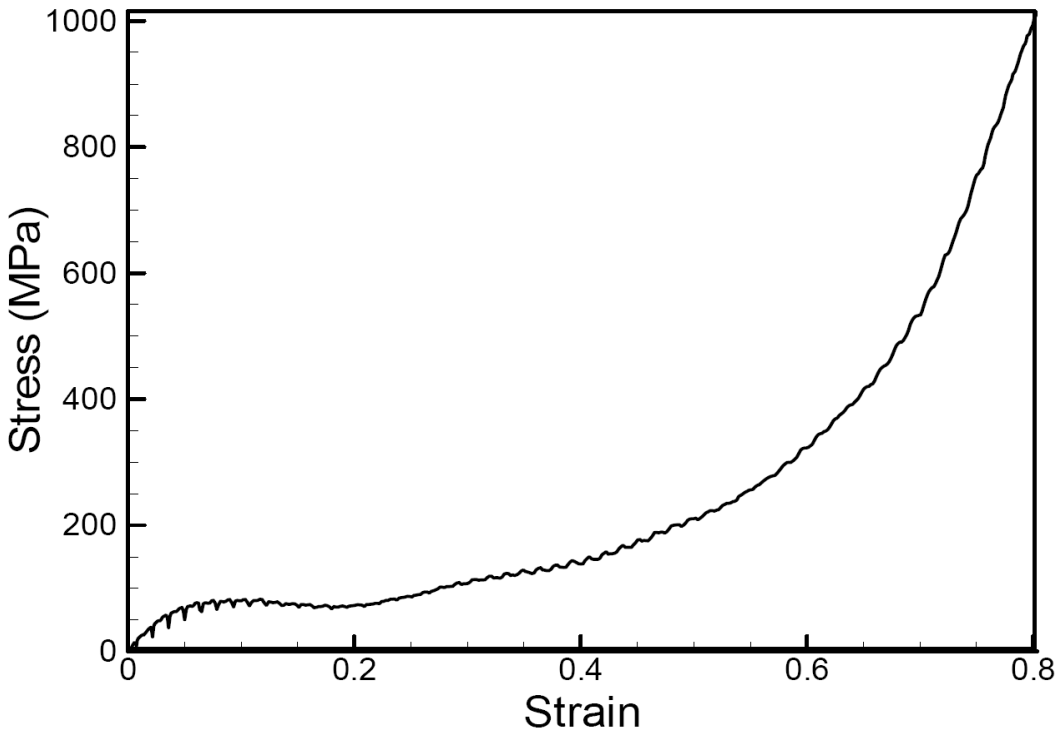


**Figure 46: GIMP stress-strain curve of the bulk metallic glass foam.**

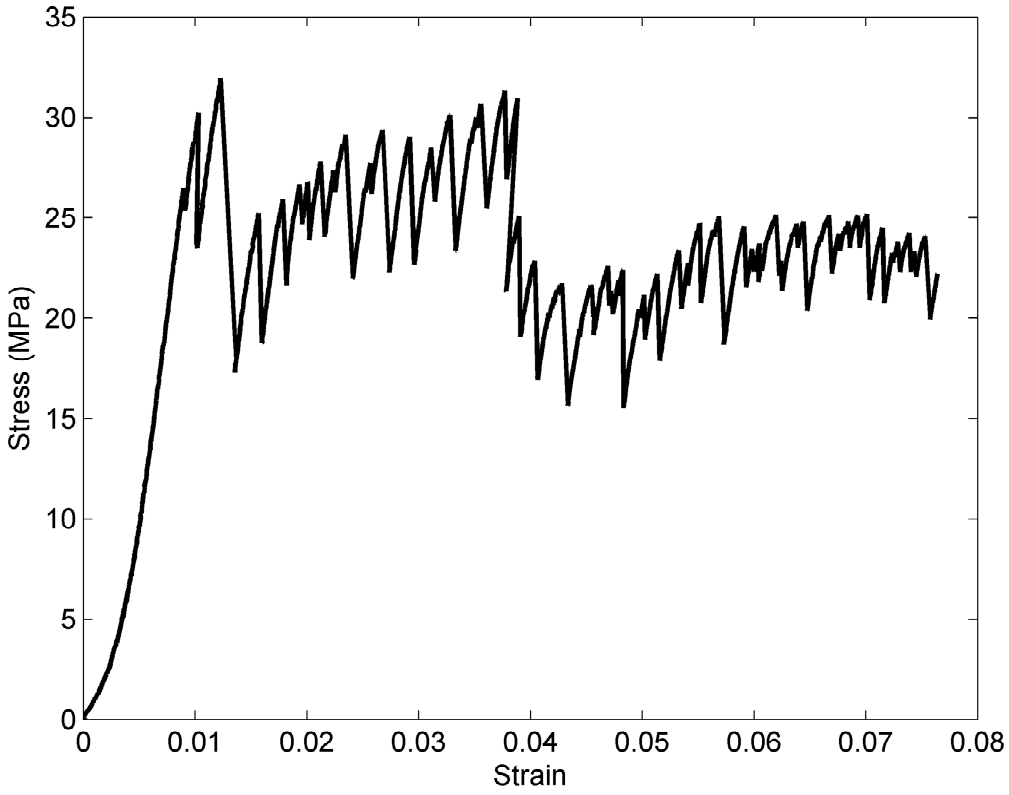


**Figure 47: Experimental stress-strain curve of BMG foam with 17% relative density.**

The GIMP stress-strain curve for the polymer foam shows very similar characteristics to that of the experimental curve which is shown in Figure 48. The only major differences between the simulated and experimental curves are the magnitude of the yield stress, plateau stress, and the onset of densification. The elastic modulus is well captured by the GIMP prediction, but the yield points, plateau stress, and densification are noticeably shifted. The offset between these three could have been influenced by the strain rates; which the simulation in GIMP was run at 1,000,000% per second, which is much higher than the 0.08% per second on the Instron machine.

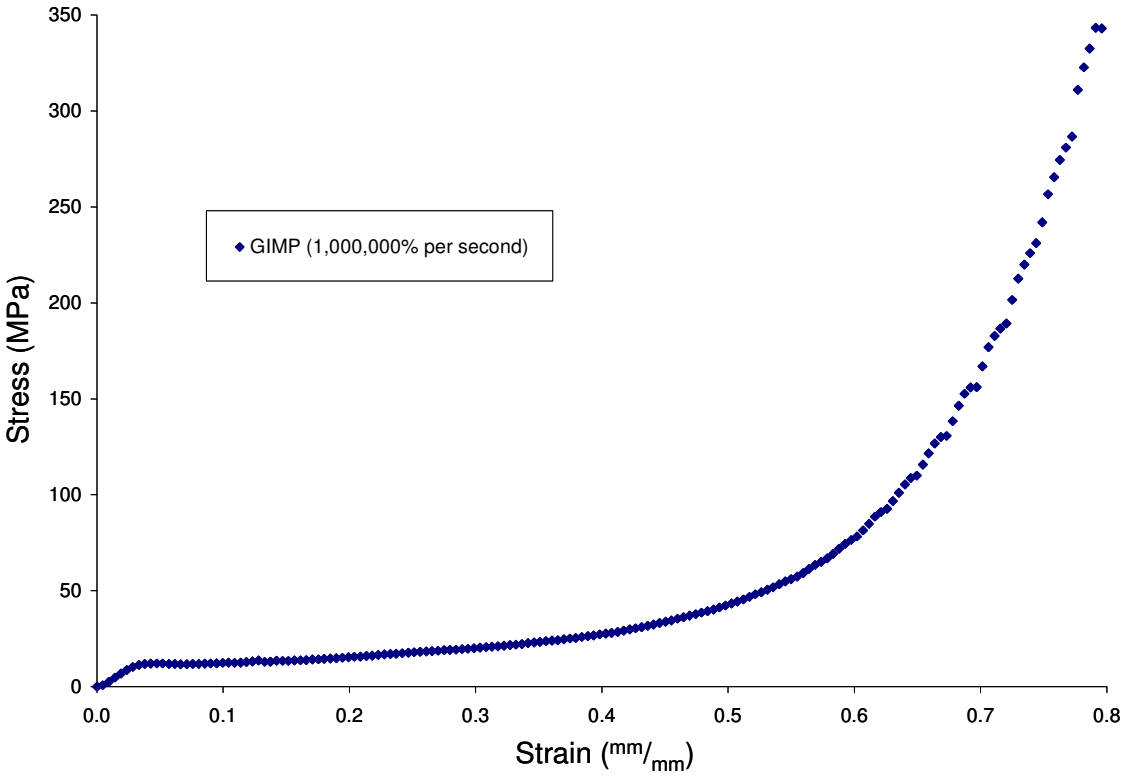


**Figure 48: GIMP stress-strain curve for the polymer foam.**

# 4 Conclusions

BMG foams can be produced via hot isostatic pressing with porosities ranging from 4% to 86%. To promote plasticity and reduce the brittleness of the foams; the porosity needs to be increased higher than the current range. Even with their brittle nature in this porosity range, BMG foams can absorb more energy than other foams. The dynamic tests, unconfined and confined, show that the BMG foams need to be confined for the maximum energy absorption.

Phase contrast in radiography and tomography enhances the edges of the cells, but make it hard to process the images for use in computational simulations such as: Digital Image Correlation and GIMP. Despite the presence of phase contrast, global strains can be measured from radiographs or tomographs using an edge detecting program. With lack of better image processing local strains have only been measured in radiographs and tomographs by hand.

*In-situ* compression of foams with radiography and tomography provides a microscopic validation for the computational simulations run in GIMP. There are agreements between the radiographs, tomographs, and GIMP microscopically, but there is room for improving the constitutive modeling.

# 5 Future Work

To improve the plasticity of BMG foams by increasing their porosities higher than 90%. Using tomographs to measure strain and track cell movements in 3-dimensions. Apply basic predictions for foams to engineer a better foam microstructure for use as blast protection. Use new processing technique to produce the custom foam microstructures such as the one shown in Figure 49.

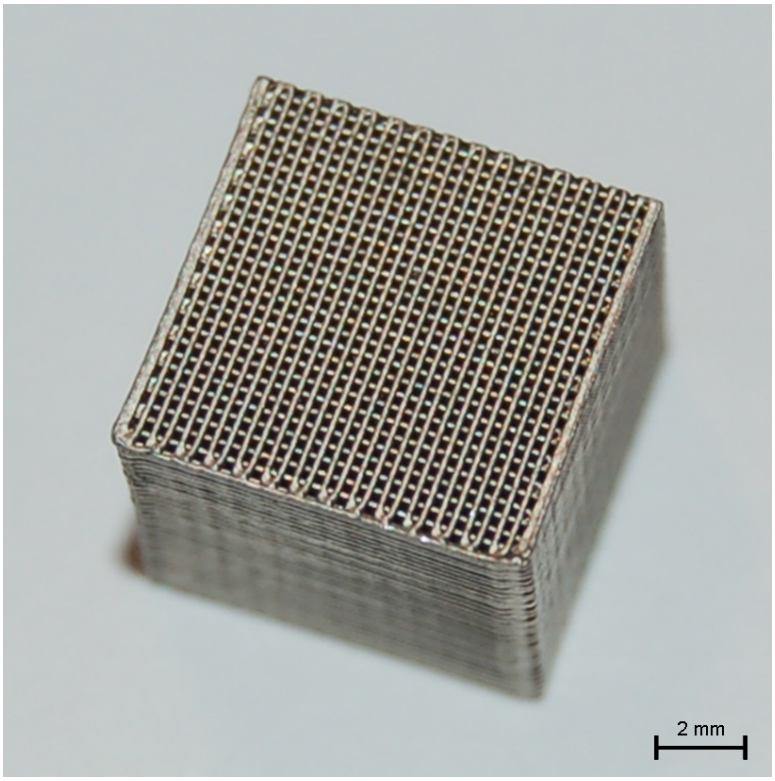


**Figure 49. Example of a Ni metal lattice produced by robocasting. The plate can be formed in simple or complex shapes with negligible effect on the processing cost (for the same volume). Thus, plate armor for extremities would also be achievable with this fabrication method. For this proposal similar structures will be designed with commercial BMG alloys or equivalent.**

# References


Ashby, M.F., Evans, A., Fleck, N.A., Gibson, L.J., Hutchinson, J.W., and Wadley H.N.G. *Metal Foams A Design Guide*. Elsevier. 2000

ASM[1] Handbook. *Volume 1. Properties and Selection: Irons, Steels, and High-Performance Alloys*. ASM International. 1999

ASTM D 1621. "Standard Test Method for Compressive Properties of Rigid Cellular Plastics." 2004

ASTM E 9. "Standard Test Methods for Compression Testing of Metallic Materials at Room Temperature." 1989

Bushberg, J.T., Seibert, A.J., Leidholdt Jr., E.M., and Boone, J.M. *The essential physics of medical imaging*. Second edition. Lippincott Williams & Wilkins. 2002. pg. 51

Callister, W.D., Jr. *Materials Science and Engineering*. 5th edition. John Wiley & Sons, Inc. 2000

Daphalapurkar, N.P., Hanan, J.C., Phelps, N.B., Bale, H., Lu, H. "Simulation and Tomography of Microstructure Evolution of a Closed-Cell Polymer Foam in Compression." To appear in Mechanics of Advance Materials and Structures (2007)

Davis, T.J., Gao, D., Gureyev, T.E., Stevenson, A.W., and Wilkins, S.W. "Phase-contrast imaging of weakly absorbing materials using hard X-rays." *Nature*; Feb 16, 1995; 373, pg. 595.

De Carlo, F. Personal Communication with. November 13 – 23 2006.

De Carlo, F. and Tieman, B.. "High-throughput X-ray microtomography system at the Advanced Photon Source Beamline 2-BM." *Proc. of SPIE* Vol. 5535. 2004

Demetriou, M.D., Hanan, J.C. Veazey, C., Di Michiel, M., Lenoir, N., Üstündag, E., and Johnson, W.L. "Yielding of metallic glass foam by percolation of an elastic buckling instability." *Advanced Materials In Press* (2007).

Demetriou, M.D., Schramm, J.P., Veazey, C., Johnson, W.L., Hanan, J.C., Phelps, N.B., "High porosity metallic glass foam: a powder metallurgy route." Submitted *Applied Physics Letters*, 2007

Demetriou, M.D., Veazey, C., Schroers, J., Hanan, J.C., and Johnson, W.L. 'Thermo-plastic expansion of amorphous metallic foams.' Journal of Alloys and Compounds. 2007.

Gibson, L.J. and Ashby, M.F. Cellular Solids: Structure and properties – Second edition. Cambridge University Press. 1997

Hanan, J.C. Diffraction for Non-destructive Materials Evaluation. MAE 5113 Lecture 5. Spring 2006

Hanan, J.C., Bale, H., and Phelps, N.B. "Materials Tester For *In-situ* Determination of Mechanical Properties Using X-ray Radiation." XXVII Oklahoma AIAA/ASME Symposium, March 31 2007

Hauck, H.-P. Rohacell. http://www.rohacell.com/en/performanceplastics8344.html. (accessed December 2007)

Liaw, P.K. TMS Conference Proceedings. cmsplus.tms.org/CMS/CMSPlus.nsf?OpenDatabase. 2008

Luo, H. "Dynamic Compressive Behavior of Bulk Metallic Glass Foam with SHPB." Unpublished. 2007.

Matweb.com 1996-2007

Merriam-Webster online dictionary. www.m-w.com. 2006-2007

Peker, A., Johnson, W.L. 'Time-temperature-transformation diagram of a highly processable metallic glass.' Material Science and Engineering A179/A180 1994, 173-175

Schroers, J., Veazey, C., Johnson, W.L. 'Amorphous metallic foam.' Applied Physics Letters. Vol. 82. Num. 3. 2003.

Wang, Y., De Carlo, F.; Mancini, D.C.; McNulty, I., and Tieman, B. 'A high-throughput x-ray microtomography system at the Advanced Photon Source.' *Review of Scientific Instruments* Vol. 72, Num. 4. 2001.

Wicklein, M. and Thoma, K. Numerical investigations of the elastic and plastic behavior of an open-celled aluminum foam. Mat. Sci. and Eng. A 397. 2005 pg. 391-399

Youssef, S., Maire, E., and Gaertner, R. Finite element modeling of the actual structure of cellular material determined by X-ray tomography. Acta Materialia 53. 2005 pg. 719-730

VITA

Nicholas B. Phelps

Candidate for the Degree of

Master of Science

Thesis: LOCAL AND GLOBAL DEFORMATION FROM SYNCROTRON IMAGING OF CLOSED CELL FOAMS IN COMPRESSION

Major Field: Mechanical Engineering

Biographical:

Personal Data:

Education:
Completed the requirements for the Bachelor of Science in Mechanical Engineering at Oklahoma State University, Stillwater, Oklahoma in May 2005.

Completed the requirements for the Master of Science in Mechanical Engineering at Oklahoma State University, Stillwater, Oklahoma in May 2008.

Professional Memberships: American Society of Mechanical Engineers (ASME)